

JGR Space Physics

RESEARCH ARTICLE

10.1029/2019JA027441

Key Points:

- Ionospheric irregularities generally occur between September and April over the South American sector
- The ROTI and S4 values indicated periods of about 2–8 days during the strong phase fluctuations probably associated with planetary waves of same period
- Adjacent plasma bubble (large-scale irregularity) separation observed by GPS ranges from ~600 to 1,000 km in the South American sector

Correspondence to:

R. de Jesus,
jesus.rodolfo@hotmail.com

Citation:

de Jesus, R., Batista, I. S., Takahashi, H., de Paula, E. R., Barros, D., Figueiredo, C. A. O. B., et al. (2020). Morphological features of ionospheric scintillations during high solar activity using GPS observations over the South American sector. *Journal of Geophysical Research: Space Physics*, 124. <https://doi.org/10.1029/2019JA027441>

Received 20 SEP 2019

Accepted 13 NOV 2019

Accepted article online 3 JAN 2020

Morphological Features of Ionospheric Scintillations During High Solar Activity Using GPS Observations Over the South American Sector

R. de Jesus¹, I. S. Batista¹, H. Takahashi¹, E. R. de Paula¹, D. Barros¹, C. A. O. B. Figueiredo¹, A. J. de Abreu^{1,2}, O. F. Jonah³, P. R. Fagundes⁴, and K. Venkatesh⁵

¹Instituto Nacional de Pesquisas Espaciais (INPE), São José dos Campos, SP, Brazil, ²Instituto Tecnológico de Aeronáutica (ITA), Divisão de Ciências Fundamentais, São José dos Campos, SP, Brazil, ³Massachusetts Institute of Technology, Haystack Observatory, Westford, MA, USA, ⁴Universidade do Vale do Paraíba/IP & D, São José dos Campos, SP, Brazil, ⁵National Atmospheric Research Laboratory, Gadanki, India

Abstract The main objective of this study is to investigate the ionospheric irregularities observed by Global Positioning System-total electron content (GPS-TEC) receivers during the high solar activity years of 2013 and 2014 at different stations in the equatorial and low-latitude regions in the South American sector. The ionospheric parameters used in this investigation are the TEC, the rate of change of the TEC index (ROTI), and the amplitude scintillation index (S4). In the South American sector, the ROTI and S4 indices showed that the ionospheric irregularities have an annual variation with maximum occurrence from September to April, between 20:00 LT and 02:00 LT, and no occurrence from May to August. Also, strong phase fluctuations (ROTI >1) are observed over South America at 19 LT in October and November. Morlet wavelet analysis of ROTI and S4 showed that planetary wave-scale periods ranging from 2 to 8 days are predominant during September–March at 20–02 LT in South America. In addition, using a keogram it was possible to evaluate the distance between adjacent ionospheric plasma depletions, and this result is presented and discussed. The longitudinal distances between adjacent bubbles vary around ~600–1000 km, which is larger than values reported in most previous studies.

1. Introduction

The ionospheric irregularities that occur in the *F* region at low and equatorial latitudes are mainly a nighttime phenomenon (Wang et al., 2008; Zou, 2011) and were first noticed by Booker and Wells (1938). These irregularities have scale sizes ranging from a few centimeters to thousands of kilometers (Abdu & Brum, 2009; Sahai et al., 1998). According to the previous studies (e.g., Fejer et al., 1999), the basic mechanism for the formation and evolution of the ionospheric irregularities is the Rayleigh-Taylor instability and the $E \times B$ instability (Abalde et al., 2009; Deng et al., 2013). As mentioned by Ram et al. (2006) and Abalde et al. (2009), some other processes that also contribute to the onset and evolution of the ionospheric irregularities are (1) the evening enhancement in the eastward electric field (Abdu et al., 2008) and rapid uplifting of the equatorial *F* region around sunset period (Fejer et al., 1999; Hoang et al., 2010; Sahai et al., 2000), (2) a sharp gradient at the base of the *F* region (Cervera & Thomas, 2006; Kelley, 1989), (3) a simultaneous decay of the *E* layer conductivity at both ends of the field line (Tsunoda, 1985), and (4) the transequatorial meridional neutral winds (Abe et al., 2018).

The irregularities are often called as “bottom side irregularities” or “equatorial ionospheric irregularities,” depending on their latitudinal extent in relation with the dip equator (Whalen, 2002). Bottom side irregularity is the plasma depletion that occurs below the *F* region maximum and because it is limited in altitude, it extends via the geomagnetic field to a narrow band in latitude perceptible only by the ionospheric sounding observation close to dip equator (Whalen, 2000, 2002). Equatorial ionospheric irregularities are the depletions that occur on the bottom side of the equatorial *F* region and rise to high altitudes and extend along the magnetic field to a wide band of latitudes and detectable by the ionospheric sounders located in the equatorial and low-latitude stations (Whalen, 1997, 2001, 2002).

There have been many investigations (Uma et al., 2012) showing the time evolution and spatial characteristics of small- or large-scale plasma depletions using ionospheric sounding data (Batista et al., 2008),

Global Positioning System (GPS) data (Muella et al., 2009, 2013), satellite measurements (Burke et al., 2004, 2012), and OI 630 and OI 777.4 nm all-sky imaging system (Paulino et al., 2011). The occurrence of the ionospheric irregularities (plasma depletions) shows large variability with solar cycle, season, geomagnetic activity, local time, and day-to-day variation (De Paula et al., 2007; Manju et al., 2016). Paulino et al. (2011) have reported that the most of the observed nights from September 2000 to April 2007 over Brazilian tropical region in South America presented plasma bubbles during 22–23 LT with drifts of 15–60 m/s. Although the seasonal and solar activity variability of the ionospheric irregularities is reasonably well understood (Manju et al., 2016), the day-to-day variability represents a continuing enigma in the modern ionospheric physics (Hajra et al., 2012; Mendillo et al., 1992).

In this paper we present a detailed investigation on the occurrence of ionospheric irregularities and scintillations at different latitudes using GPS observations over the South American sector during the high solar activity (HSA) years of 2013 ($\langle F_{10.7} \rangle = 123$) and 2014 ($\langle F_{10.7} \rangle = 146$). Wavelet analysis has been carried out to find out the periodicities in the occurrence of ionospheric scintillations during different local times and their association with planetary wave activity. Also, adjacent plasma bubble separation has been calculated using different GPS networks over the entire South American region and corresponding results are presented and discussed in the following sections.

2. Data Analysis

The GPS observations obtained from seven GPS receiving stations in the South American sector (SALU, IMPZ, PAL, BRAZ, MGRP, CHPI, and POAL; see Figure 1a and Table 1) during 2013 and 2014 have been used to calculate the vertical total electron content (VTEC) and rate of change of total electron content (TEC) index (ROTI). Figure 1a and Table 1 present the details of these GPS stations. The dip latitudes presented in Table 1 were calculated for the year 2014, at an altitude of 300 km, using International Geomagnetic Reference Field-12 (Thébault et al., 2015). The VTEC and ROTI data from São Paulo (POLI; 26°S, 45°W) station have also been used to complement few days of missing data at Cachoeira Paulista (CHPI). Also, measurements of scintillations (S4 index and amplitude scintillation index) from São Luís (SALU) and CHPI during 2013 and 2014 are presented. The S4 index measurements from São José dos Campos (23.1°S, 45.8°W) have also been used to complement few days of missing data at CHPI. These stations mentioned earlier belong to the Brazilian Network of “Rede Brasileira de Monitoramento Contínuo dos Sistemas (RBMC) Global Navigation Satellite System (GNSS)”, Low-Latitude Ionospheric Sensor Network (LISN), or “Instituto Nacional de Pesquisas Espaciais.”

The slant TEC (STEC) is described as the integral of the electron density from GPS receiver to satellite (Bires et al., 2016; Cherniak & Zakharenkova, 2017) along the satellite raypath that is computed in units of TEC (1 TEC unit = 10^{16} electrons/m²).

The STEC is converted into VTEC using the following relation (Rao et al., 2006):

$$\text{VTEC} = [\text{STEC} - (b_R + b_S)] / S(\phi) \quad (1)$$

where b_R is the interfrequency differential receiver biases, b_S is the interfrequency differential satellite biases, ϕ is the elevation angle of the GPS satellite, $S(\phi)$ is the mapping function with zenith angle β at the ionospheric pierce point (IPP). The mapping function is obtained by the following relation (Mannucci et al., 1993; Langley et al., 2002; Rao et al., 2006):

$$S(\phi) = \frac{1}{\cos(\beta)} = \left[1 - \left(\frac{R_E \times \cos(\phi)}{R_E + H_S} \right)^2 \right]^{-1/2} \quad (2)$$

where R_E is the mean Earth's radius and H_S is the IPP altitude.

The rate of change of TEC index (ROTI) detects the presence of the ionospheric irregularities at scale lengths of a few kilometers (Basu et al., 1999; Cherniak & Zakharenkova, 2017). ROTI (5-min standard deviation of ROT) can be expressed as (Cherniak & Zakharenkova, 2017; Pi et al., 1997):

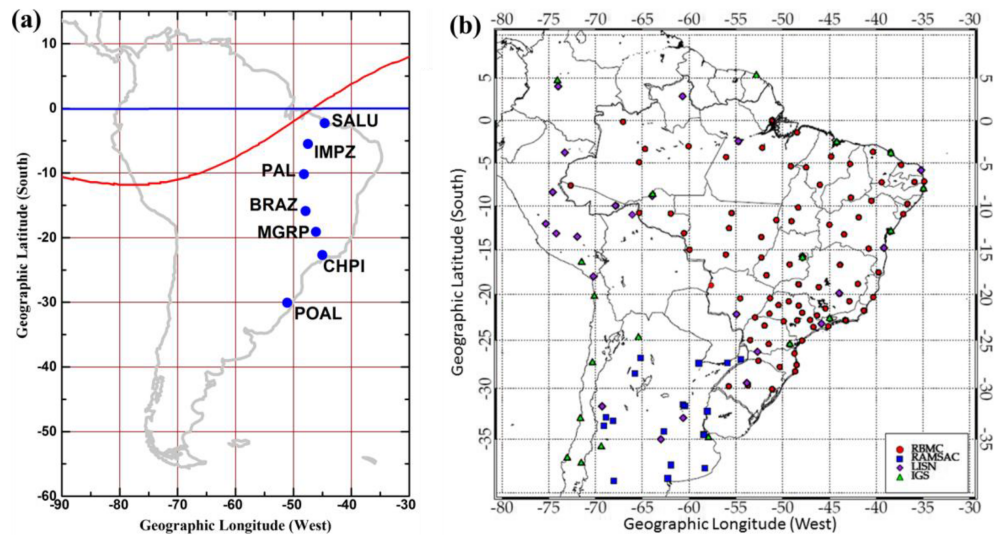


Figure 1. (a) Map showing the locations of the GPS receivers (SALU, IMPZ, PAL, BRAZ, MGRP, CHPI, and POAL) over the South American sector. The geographic equator (blue colored line) and geomagnetic equator (red colored curve) are also shown. (b) Map showing the locations of the GPS stations over the South American sector used to calculate TEC maps and the distance between adjacent plasma bubbles.

$$ROTI = \sqrt{\langle ROT^2 \rangle - \langle ROT \rangle^2} \quad (3)$$

$$ROT = \frac{\Delta STEC}{\Delta t} \quad (4)$$

where $\Delta STEC$ is the difference between the STEC values at two successive times at the time interval (Δt). Only STEC data from satellites whose elevation angles were larger than 35° were used in equation (4) to minimize the multipath errors (Buhari et al., 2014; Ma & Maruyama, 2006). ROT is computed in units of TECU/min.

The strength of amplitude scintillations at GPS L1 frequency (1575.42 MHz) is given by the S4 index (Aggarwal et al., 2013; Dashora & Pandey, 2005; Yeh & Liu, 1982):

$$S_4 = \sqrt{\frac{\langle I^2 \rangle - \langle I \rangle^2}{\langle I \rangle^2}} \quad (5)$$

where the brackets $\langle \rangle$ represent time average values computed for each 1-min period and I is the intensity of the received signal. The S4 values are computed for all satellites with elevation angles over 35° . The ionospheric irregularities sampled by ROTI and S4 index will correspond to the scale sizes of about 6 km and 400 m, respectively (Basu et al., 1999; Tanna & Pathak, 2014; Zou & Wang, 2009).

Table 1
Coordinates of the GPS Receivers at SALU, IMPZ, PAL, BRAZ, MGRP, CHPI, and POAL

Location	Symbol used (Network) *	Geog. lat.	Geog. long.	Dip. lat.
São Luís, Brazil	SALU (RBMC/LISN/INPE)	02.3°S	44.6°W	02.84°S
Imperatriz, Brazil	IMPZ (RBMC)	05.5°S	47.5°W	04.10°S
Palmas, Brazil	PAL (RBMC)	10.2°S	48.2°W	07.86°S
Brasília, Brazil	BRAZ (RBMC)	15.9°S	47.9°W	12.88°S
Rio Paranaíba, Brazil	MGRP (RBMC)	19.2°S	46.1°W	16.58°S
Cachoeira Paulista, Brazil	CHPI (RBMC/LISN/INPE)	22.7°S	45.0°W	19.88°S
Porto Alegre, Brazil	POAL (RBMC)	30.1°S	51.1°W	21.95°S

Note. RBMC = Rede Brasileira de Monitoramento Continuo dos sinais GPS; LISN = Low Latitude Ionospheric Sensor Network; INPE = Instituto Nacional de Pesquisas Espaciais.

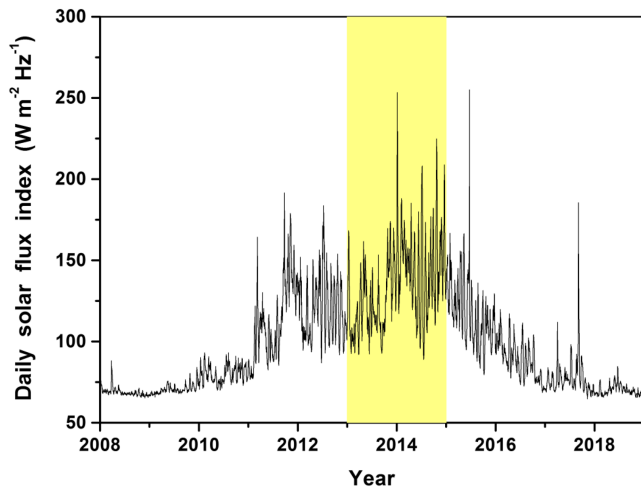


Figure 2. The 10.7-cm solar flux index variations during 2008–2018 (solar cycle 24). The yellow background portion highlights the period between January 2013 and December 2014.

The continuous wavelet transform (CWT) is applied for the S_4 and ROTI values for years 2013 and 2014. The CWT provides an excellent balance between time and frequency positions. Given a discrete sequence $m_u(u = 1 \dots N)$ with uniform time steps dt , a CWT is defined as the convolution of m_u with a scaled and shifted version of the mother wavelet ϕ_0 (Divine & Godtlielsen, 2007; Grinsted et al., 2004; Torrence & Compo, 1998):

$$W_{UL}^L(s) = \sqrt{\frac{dt}{s}} \sum_{u'=1}^N m_{u'} \phi_0 \left[\frac{(u' - u)dt}{s} \right] \quad (6)$$

$$\phi_0 = \pi^{-1/4} e^{j\omega_0\eta - 0.5\eta^2} \quad (7)$$

where s is the wavelet scale, j is the imaginary symbol of complex number, η is a nondimensional “time” parameter, and $\omega_0 = 6$ is the nondimensional frequency. The wavelet power and local phase are defined as $|W_{UL}(s)|^2$ and the complex argument of $W_{UL}(s)$, respectively (Grinsted et al., 2004).

Also, the distance between adjacent ionospheric bubbles over South America for years 2013 and 2014 has been investigated using TEC map based on GPS receivers shown in Figure 1b. The GPS receivers used in this study belong to the RBMC, LISN, Argentinian Network of Continuum Monitoring of Satellites, and International GNSS Service. The methodology applied to generate the TEC map was described in detail by Takahashi et al. (2015, 2016) and Barros et al. (2018): (1) TEC data were mapped on the ionospheric shell at an altitude of 350 km with a pixel size of $0.5^\circ \times 0.5^\circ$ in latitude and longitude; (2) to compensate for the scarcity of the TEC data distribution, we first computed a running average of 3×3 elements, which corresponds to approximately $150 \times 150 \text{ km}^2$; (3) if no data were found in the area, the running average area expands to 5×5 elements (this corresponds an area of $\sim 250 \times 250 \text{ km}^2$); and (4) if the problem persists, the running average elements expand up to 21×21 elements ($\sim 1000 \times 1000 \text{ km}^2$). Using the TEC maps, we calculated the distance between adjacent bubbles employing keogram technique (Barros et al., 2017). A keogram is a longitude versus time plot created from a collection of west-east slices of TEC maps at a fixed latitude (Barros et al., 2018). The distance between adjacent ionospheric plasma bubbles was computed by the longitudinal distance of the plasma bubble (Barros et al., 2017). This method has been well validated by Barros et al. (2017, 2018) using a large number of GPS receivers over South America. Therefore, in order to maintain the same quality of the results obtained by Barros et al. (2017, 2018), in this work we calculate the distance between adjacent bubbles using different GPS networks over the entire South American sector. This methodology was applied from ~ 0 to $\sim 35^\circ\text{S}$ latitudes and from 35°W to 75°W longitudes.

Figure 2 shows the $F_{10.7}$ index variations from January 2008 to December 2018 obtained from <https://omniweb.gsfc.nasa.gov/form/dx1.html> website. The yellow rectangle highlights the period investigated between January 2013 and December 2014. The period used has maximum solar activity, with $F_{10.7}$ ranging from 89 to 253. The mean $F_{10.7}$ values for years 2013 and 2014 were about 123 and 146, respectively.

3. Results and Discussion

3.1. Occurrence of Scintillation Using ROTI and S_4 index

Figure 3a shows the plots of hourly average ROTI index (phase fluctuations) as a function of day of year (DOY) and geographic latitude ($0\text{--}30^\circ\text{S}$) using seven GPS-TEC stations (SALU, IMPZ, PAL, BRAZ, MGRP, CHPI, and POAL) over $\sim 45^\circ$ to 50°W in South America during 2013 (HSA). The ROTI values at each GPS station are interpolated. The spatial distributions of the IPPs for all visible GPS satellites over a single station during 24 h (not shown here) cover about 8° in latitude (Cherniak et al., 2018). The nine panels in Figure 3a show the hourly mean values of ROTI at each hour from 19 LT (22 UT) to 03 LT (06 UT). Figure 3b is similar to Figure 3a but for 2014 (solar activity for 2014 was higher than 2013). The hourly average of ROTI for 04, 05, and 18 LT (not shown here) during 2013 and 2014 showed value lower than 0.2 (ROTI

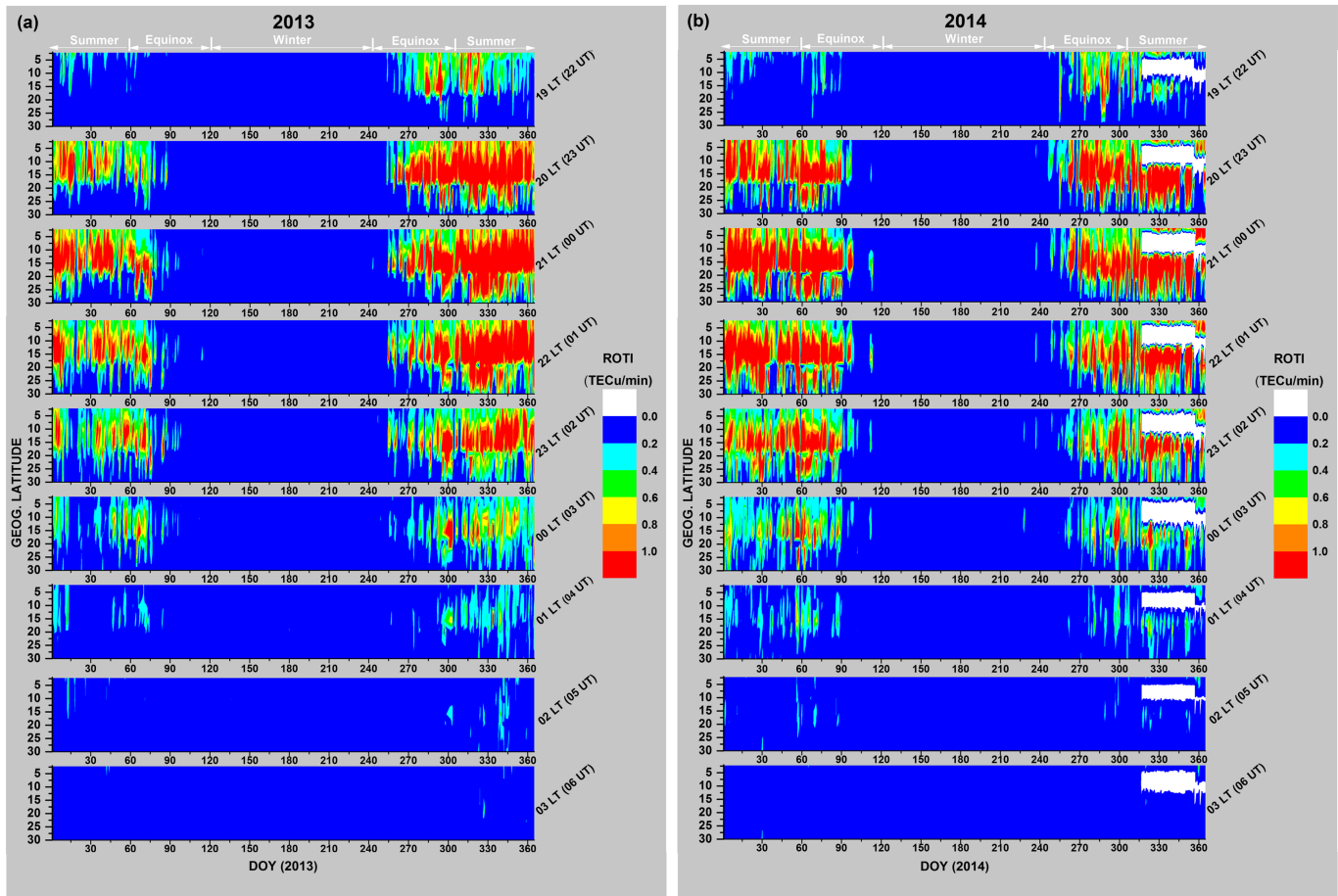


Figure 3. (a) ROTI index plots as a function of DOY (day of year) and latitude (from 0 to 30 S) using seven GPS-TEC stations ($\sim 45^\circ\text{W}$), during 2013 (HSA). The nine panels show the hourly mean ROTI data obtained for the seven stations from 19:00 LT (22:00 UT) to 03:00 LT (06:00 UT). (b) Same as Figure 3a but for 2014. The white color indicates no data.

<0.2 is considered to be a noise). With the aim of analyzing ROTI and S4 index during 2013 and 2014 for SALU and CHPI, these parameters are presented in Figures 4 and 5, respectively. The white color in Figures 3–5 indicates no data.

Figures 3a, 3b, 4a, 4b, 5a, and 5b show ionospheric irregularities ($\text{ROTI} > 0.2$; $S4 > 0.15$) predominantly between ~ 20 LT and ~ 02 LT during the equinox months (March, April, September, and October) and summer months (November to February) over equatorial and low-latitude stations in South America. ROTI and S4 indices from GPS observations (see Figures 3a, 3b, 4a, 4b, 5a, and 5b) show no ionospheric irregularities in winter months (May–August) in the South American sector. In winter, the ROTI and S4 values are very low. De Paula et al. (2019) suggested that the background noise value of ionospheric irregularities has an S4 value of <0.15 . In the present investigation, $\text{ROTI} < 0.2$ and $S4 < 0.15$ are considered to be at noise level, since these values are predominant even in the daytime (not shown here) between 06 and 18 LT during which the irregularities are not present in general. Sobral et al. (2002) studied the ionospheric irregularities observed by the 630-nm airglow photometers at CHPI (low-latitude station), Brazil (South America), during the period of 1977–1988. They reported that the maximum occurrence of plasma bubbles extends from September through April for HSA. However, according to Sobral et al. (2002), during low solar activity (LSA) the period of largest occurrence of ionospheric irregularities is restricted between October and March. They also pointed out that the months of May–August showed the minimum of occurrence of plasma depletions for both HSA and LSA periods. Using data recorded by GPS receivers at CHPI during September 1997 to November 2014, Muella et al. (2017) reported that the occurrence of L band scintillations follows the seasonal distribution of plasma bubbles detected over eastern South America. Our results show maximum

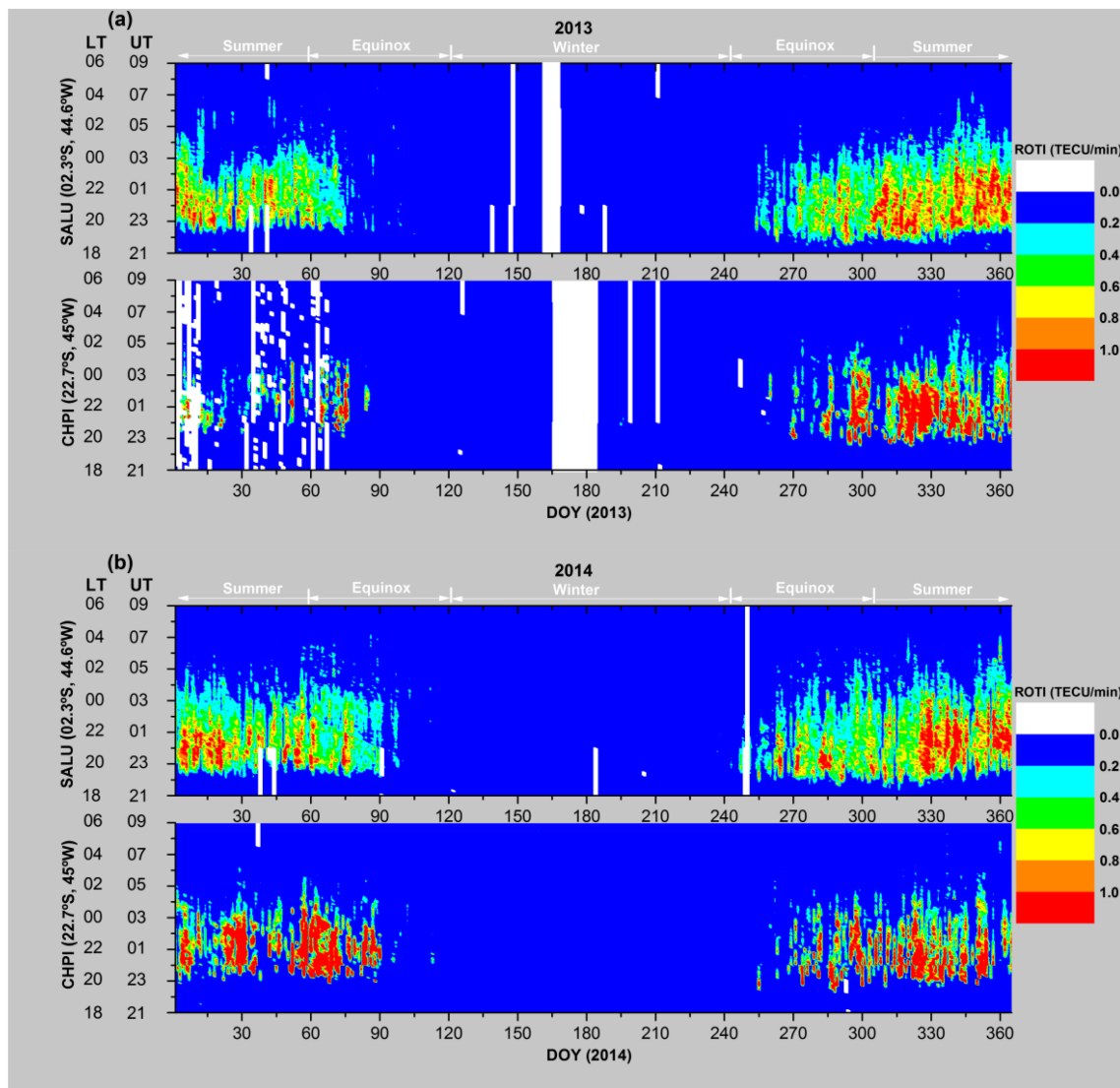


Figure 4. (a) ROTI variations with UT as a function of DOY (1 January 2013 to 31 December 2013) at SALU and CHPI. The white color indicates no data. (b) Same as Figure 4a but for 2014.

values of ROTI and S4 indices at CHPI from September to April and minimum values between May and August during the period of HSA (2013–2014) in solar cycle 24, which confirms the results of Sobral et al. (2002) and Muella et al. (2017). Abdu et al. (1981) and Batista et al. (1986, 1996) reported that the evening ionospheric *F* region vertical drift prereversal peak has lowest amplitudes in winter and highest in equinoxes and summer months in the Brazilian sector. In general, the highest (lowest) ionospheric irregularities occurrence rates are associated with larger (smaller) amplitude of the evening ionospheric *F* layer plasma vertical drift prereversal peak leading to an amplified (reduced) growth rate of the Rayleigh-Taylor instability (Abdu et al., 1981; Muella et al., 2009).

Sripathi et al. (2011) have investigated the development of equatorial spread-*F* irregularities over the Indian sector using multi-instrument observations during LSA in solar cycle 23 and reported an equinoctial asymmetry in both the occurrence of scintillations and ROTI wherein their occurrence is greater in the vernal equinox than in the autumn equinox. Using VHF and GPS receivers in Kenya during 2011, Olwendo et al. (2013) also reported that an equinoctial asymmetry in scintillation occurs with higher occurrence in March–April than in September–October. In the present work, the results from Figures 3a, 3b, 4a, 4b, 5a, and 5b also reveal an equinoctial asymmetry in the occurrence of the ionospheric irregularities with

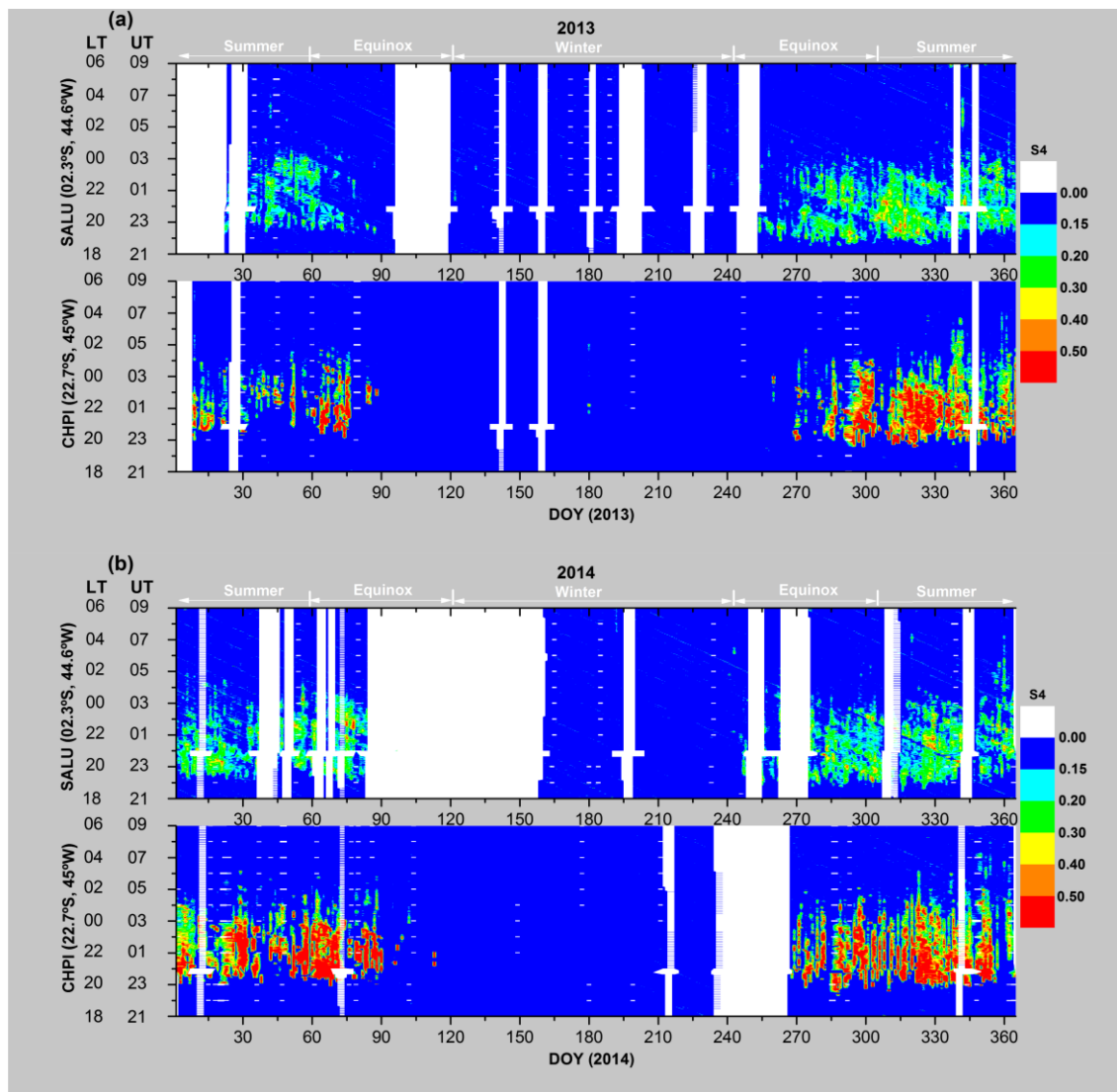


Figure 5. (a) S4 variations at SALU and CHPI during DOY 01–365 (2013). The white color indicates no data. (b) Same as Figure 5a but for 2014.

higher occurrence in September–October than in March–April. According to Otsuka et al. (2006) and Olwendo et al. (2013), an equinoctial asymmetry in the occurrence of the ionospheric irregularities could be associated to the equinoctial asymmetry of the zonal neutral winds in the thermosphere that drives the eastward electric fields (Sripathi et al., 2011).

One of the most interesting observations from Figures 3a and 3b are the unusual distribution of ionospheric irregularities at 19 LT (22 UT) during 2013 and 2014. At this time, in general, equatorial ionospheric irregularities up to ~15°S were observed in September–January (on 270–360 and DOY 01–30) and March, with higher values of ROTI in October–November (on DOY 285–330). In addition, Figures 3a and 3b show weak level of phase fluctuations (ROTI index <0.4) in January and March at 19 LT. Figure 6 presents the ROTI variations during the early evening hours (18 LT–20 LT) in South America as a function of time (LT) and DOY at SALU (near-equatorial station) and PAL (low-latitude station) for year 2013. We did not generate the figures of the ROTI values between 18 LT and 20 LT for year 2014 because of the lack of data at PAL during November–December. Figure 6 shows that the initial time of the phase fluctuation near equatorial station (SALU) is around 19:15 LT, 19:30 LT, and 18:45 LT in December–January, February–March, and September–November, respectively. The phase fluctuations at the low-latitude station (PAL) occur around 15 min after of the formation of the ionospheric irregularities near the equatorial region. Although other

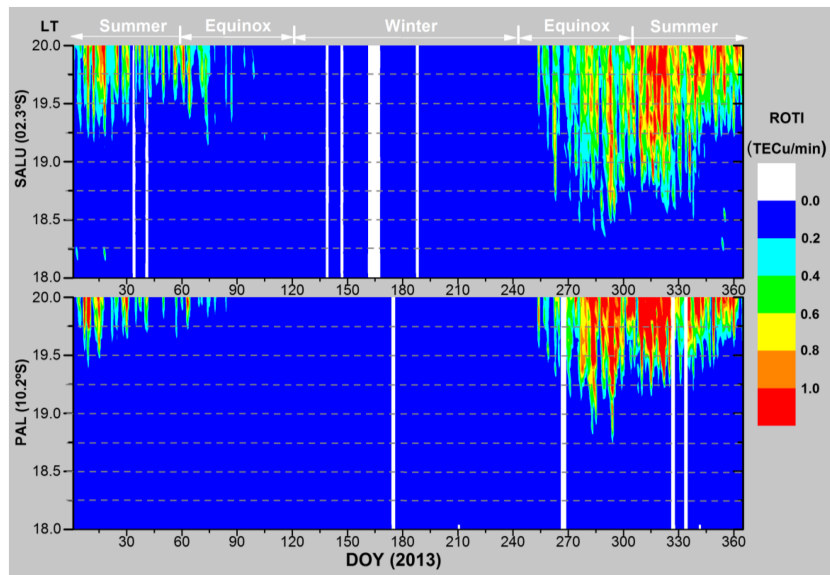


Figure 6. ROTI variations between 18 LT and 20 LT with LT as a function of DOY (2013) at SALU and PAL. The white color indicates no data.

studies (e.g., Sobral et al., 2002) have shown that ionospheric irregularities normally occur between September and April during HSA in the South American sector ($\sim 45^\circ\text{W}$), the present results during 2013 and 2014 (HSA) show that in the early evening hours (at 19 LT) strong phase fluctuations ($\text{ROTI} > 1$) occur predominantly in October–November (see Figures 3a and 3b). It should be mentioned that the maximum solar activity in previous solar cycles was much larger than 2013–2014. The main physical phenomena involved in the formation of irregularities were described previously. However, more studies are needed to improve our knowledge about the generation of ionospheric irregularities in the early evening hours over the South American sector. Possible effect of the planetary wave activity on the development of ionospheric irregularities is discussed in the next section.

The hourly averages of VTEC from 18 to 05 LT (nighttime) are shown in Figures 7a and 7b as a function of DOY and latitude (from 0° to 30°S) using seven GPS receivers in the South American sector ($\sim 45^\circ\text{W}$) during 2013 and 2014, respectively. The white color in Figures 7a and 7b indicates no data.

In Figures 7a and 7b it is possible to identify the nighttime equatorial ionization anomaly (EIA) behavior during 2013 and 2014, respectively. The equatorial anomaly region of the Earth's ionosphere (widely called as EIA) is characterized by crests near $\pm 15^\circ$ magnetic latitude with lesser electron density at the magnetic equator (Aggarwal et al., 2012; Appleton, 1946; Balan et al., 1995; Huang et al., 2014). According to Moffett and Hanson (1965) and Anderson (1973), the EIA is generated by combined effects of $\vec{E} \times \vec{B}$ drift and ambipolar diffusion. When the equatorial plasma is elevated to higher altitudes, it diffuses away from the magnetic equator along the geomagnetic field lines under the influence of the gravity and the pressure gradient forces (Anderson, 1973; Balan et al., 2018; Khadka et al., 2018; Stolle et al., 2008; Watthanasangmechai et al., 2015; Zhang et al., 2009).

The results shown in the panels of Figures 7a and 7b reveal that, for years 2013 and 2014, the EIA crest (around $15\text{--}20^\circ\text{S}$) is strong in equinox and summer months between 18 LT and ~ 01 LT, with the stronger anomaly crest during equinoctial months. A possible explanation for this seasonal variation of the EIA crest is the change of direction of neutral wind (Balan et al., 2018; Liu et al., 2013). According to Balan et al. (2018), the neutral wind makes the equatorial plasma fountain asymmetric and provides more ionization to the hemisphere of poleward wind. The stronger plasma fountain transfers more plasma to the anomaly crest regions (Trivedi et al., 2011). During the equinoxes, meridional winds flow from the equator toward the poles, resulting in a high ionization crest value (Liu et al., 2013; Zhenzhong et al., 2012). It is observed (see Figures 7a and 7b) that the anomaly crest is weak during winter over the South American sector.

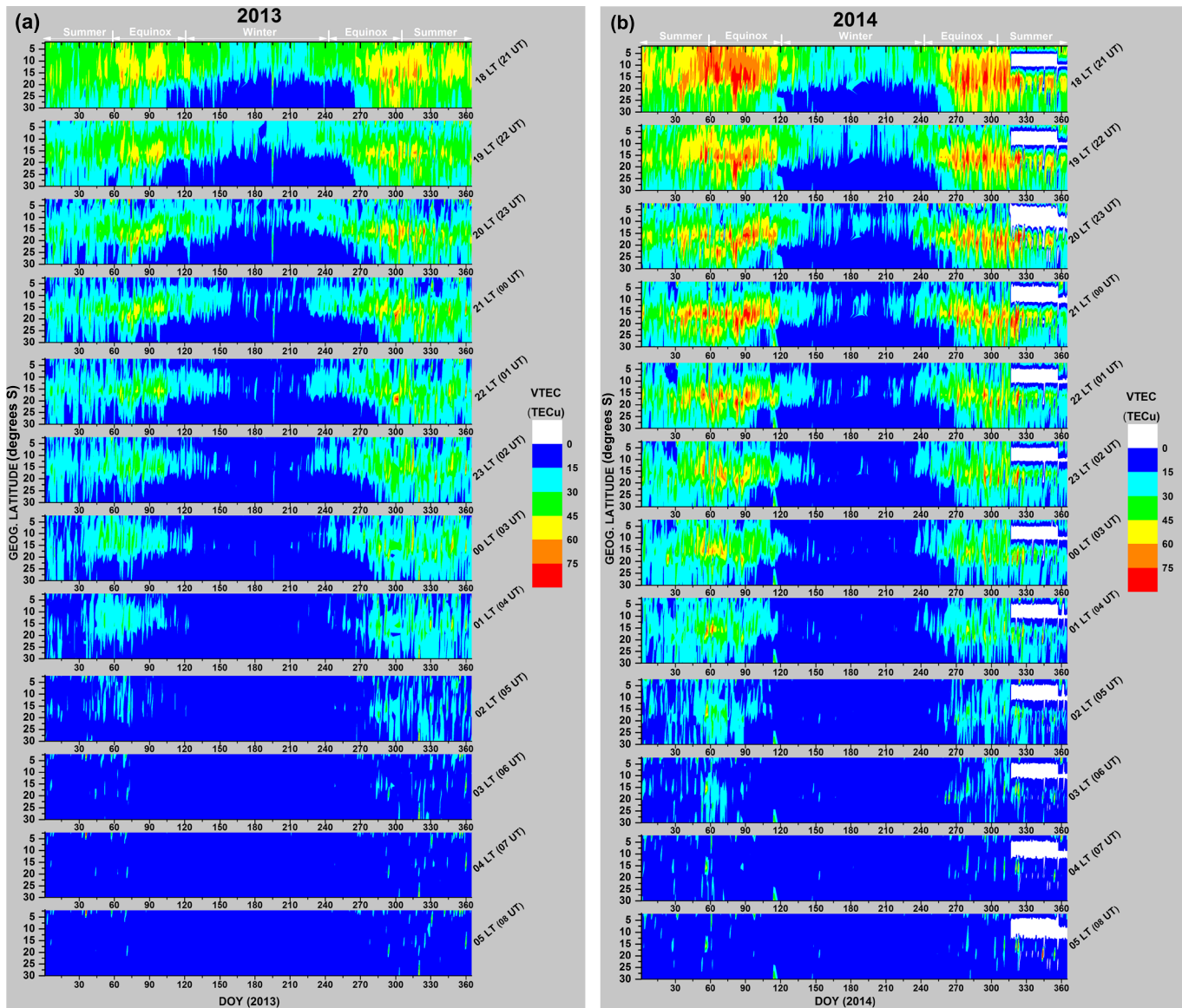


Figure 7. (a) VTEC plots as a function of DOY (day of year) and latitude (from 0 to 30 S) using seven GPS-TEC stations ($\sim 45^\circ\text{W}$), during 2013 (HSA). Each panel shows the hourly mean VTEC data obtained for the seven stations from 18:00 LT (21:00 UT) to 05:00 LT (08:00 UT). (b) Same as Figure 7a but for 2014. The white color indicates no data.

The results shown in the panels of Figures 3a, 3b, 4a, 4b, 5a, and 5b reveal a clear occurrence of ionospheric irregularities between September and March, with strong amplitude scintillation ($S_4 > 0.5$) and phase fluctuations ($\text{ROTI} > 1$) centered around the EIA crest region. Basu and Basu (1983) and Whalen (2009) have investigated the occurrence of the ionospheric scintillations in the equatorial and anomaly region, using the data from the Marisat satellite and Ascension Island (8.0°S , 14.4°W). They have reported that the ionospheric scintillations are caused by the ionospheric plasma bubbles. Whalen (2009) has pointed out that the strength of the scintillation is determined by magnitude of the electron density that the ionospheric plasma bubble intersects. According to Basu and Basu (1983), strong levels of scintillations are related with ionospheric plasma bubbles having large depletions the ones that are immersed in a background of high ambient electron density. However, recent works (Bhattacharyya et al., 2014, 2017) suggested that the irregularity spectrum is also important to determine the strength of the ionospheric irregularities. Bhattacharyya et al. (2017) reported that the irregularity spectrum at the EIA crest is shallower than that in the equatorial region. They also demonstrated that the higher

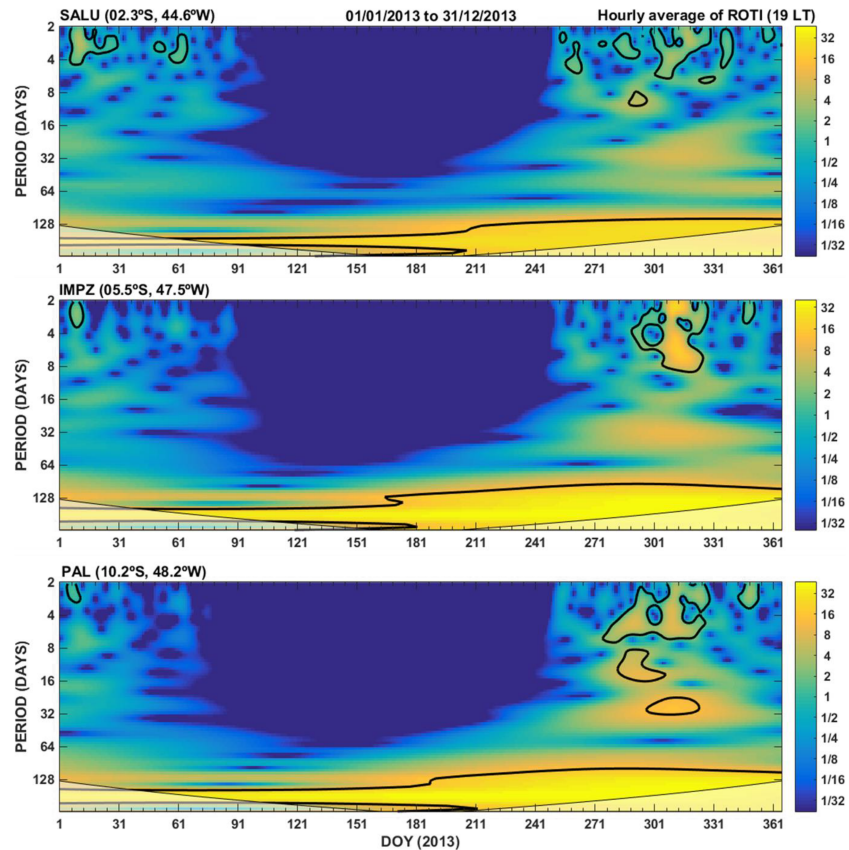


Figure 8. Wavelet transform applied in the hourly average of ROTI between 19 LT and 19:59 LT for SALU, IMPZ, and PAL during 2013.

background electron density in the ionospheric *F* region at the EIA crest would not generate strong levels of scintillations unless the irregularity there was sufficiently shallow.

3.2. Periodicities in the Scintillation Occurrence

CWT analysis was employed to check the periodicities of the ROTI at 19 LT and 20–02 LT. Figure 3 shows ionospheric irregularities up to $\sim 10\text{--}15^\circ\text{S}$ at 19 LT. In the present section, we used data from SALU, IMPZ, and PAL to investigate the main periodicities of the ROTI during these irregularities in the evening hours (19 LT). Figure 8 shows the wavelet plots of hourly average of ROTI (between 19 LT and 19:59 LT) for the station of SALU, IMPZ (near-equatorial stations), and PAL (low-latitude station) during 2013. We did not generate the wavelet plots of the hourly mean ROTI at 19 LT during 2014 because of the lack of data at IMPZ and PAL in November and December. Figures 9a and 9b show the wavelet analysis distribution of daily average of ROTI (SALU and CHPI) during nighttime (between 20 and 02 LT) for years 2013 and 2014, respectively. Figures 10a and 10b show the wavelet plots of daily average of S4 (SALU and CHPI) during night hours (20–02 LT) for years 2013 and 2014, respectively. It should be mentioned that SALU and CHPI are the same stations used to analyze ROTI and S4 index (during 20–02 LT) in Figures 4 and 5, respectively. The white color in Figures 9 and 10 indicates no data. The thick black contour is the 5% significance level against random noise (Casty et al., 2007). The lighter shade delineates the cone of influence (Girardin et al., 2006).

During the strong phase fluctuations ($\text{ROTI} > 1$; see Figure 3a) observed at 19 LT on DOY $\sim 280\text{--}331$ in year 2013, the 5% significance regions of the power (see the thick black contour in Figure 8) indicate periods of $\sim 02\text{--}08$ day in ROTI at SALU, IMPZ (near-equatorial stations), and PAL (low-latitude station). The thick black contours at PAL in Figure 8 also show the presence of oscillations with periods of about 8–16 and 16–32 days during DOY 280–300 and DOY 301–331, respectively. On DOY $\sim 331\text{--}360$, $\sim 02\text{--}31$, and $\sim 59\text{--}65$ of 2013 at 19 LT, during the moderate or weak level of phase fluctuations ($0.2 <$

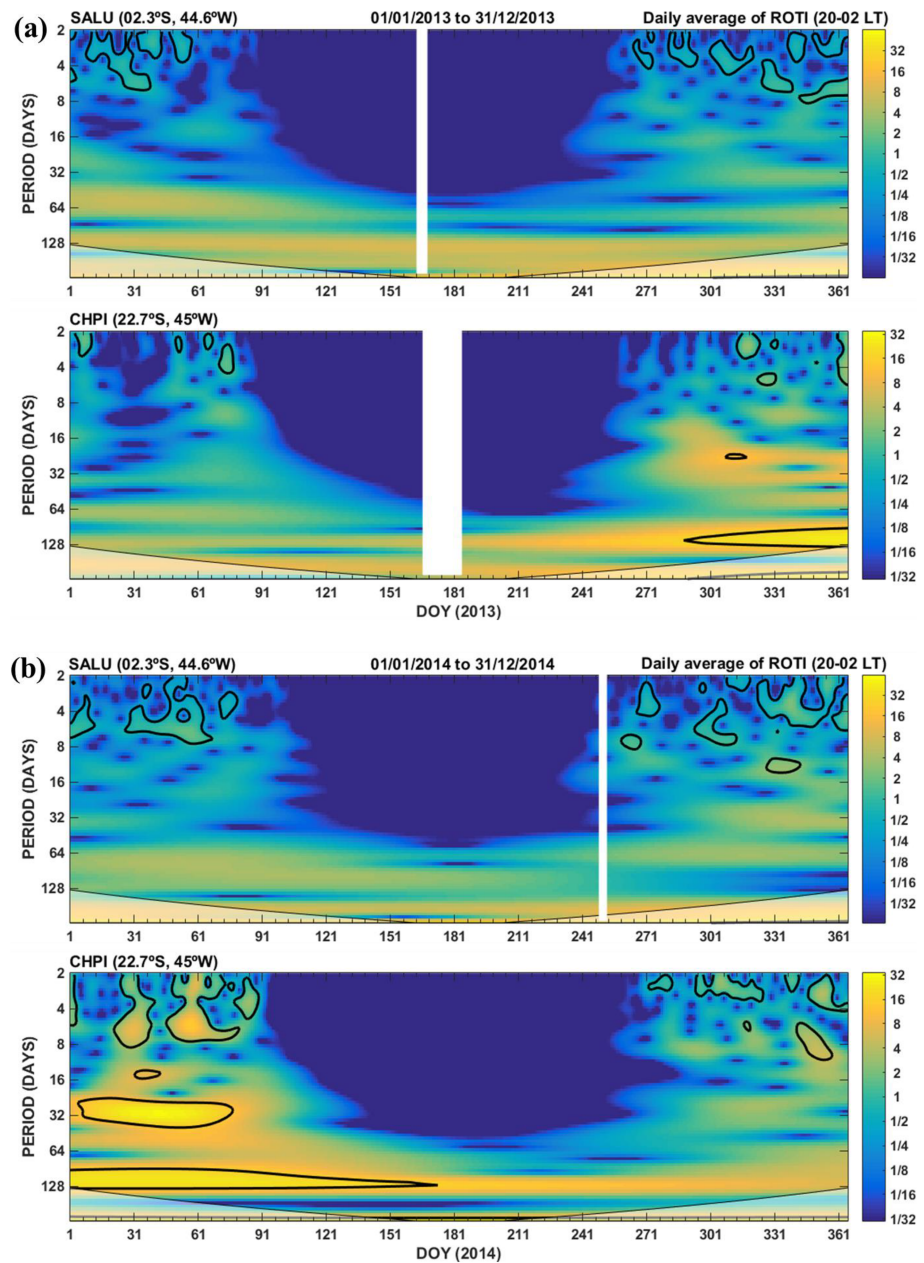


Figure 9. (a) Wavelet transform applied in the daily average of ROTI during nighttime (between 20 and 02 LT) of DOY 01 to 365 in year 2013. The white bars indicate no data. (b) Same as Figure 9a but for 2014.

ROTI index <1 ; see Figure 3a), the thick black contour in Figure 8 shows periods of 02–04 day in ROTI at SALU, IMPZ, or PAL. Apart from the periodicities highlighted by the thick black contours, the results presented in Figure 8 reveal the presence of stronger periods of ~16–32 days at SALU, IMPZ, and PAL on DOY ~271–361.

In general, the wavelet analysis distribution of daily average of ROTI (Figures 9a and 9b) and S4 (Figures 10a and 10b) between 20 LT and 02 LT (see the thick black contours) shows that the period of ~02–08 days is very intense at SALU (near-equatorial station) and CHPI (low-latitude station) on DOY ~270–90 in 2013 and 2014. As mentioned earlier, the ionospheric irregularities in the South American sector (~45°W) occurred between 20 LT and 02 LT during DOY 270–90 (see Figures 3a, 3b, 4a, 4b, 5a, and 5b). The thick black contour at CHPI in Figure 9b also shows periods of ~16–32 days in ROTI (20–02 LT) on DOY ~01–80 in 2014.

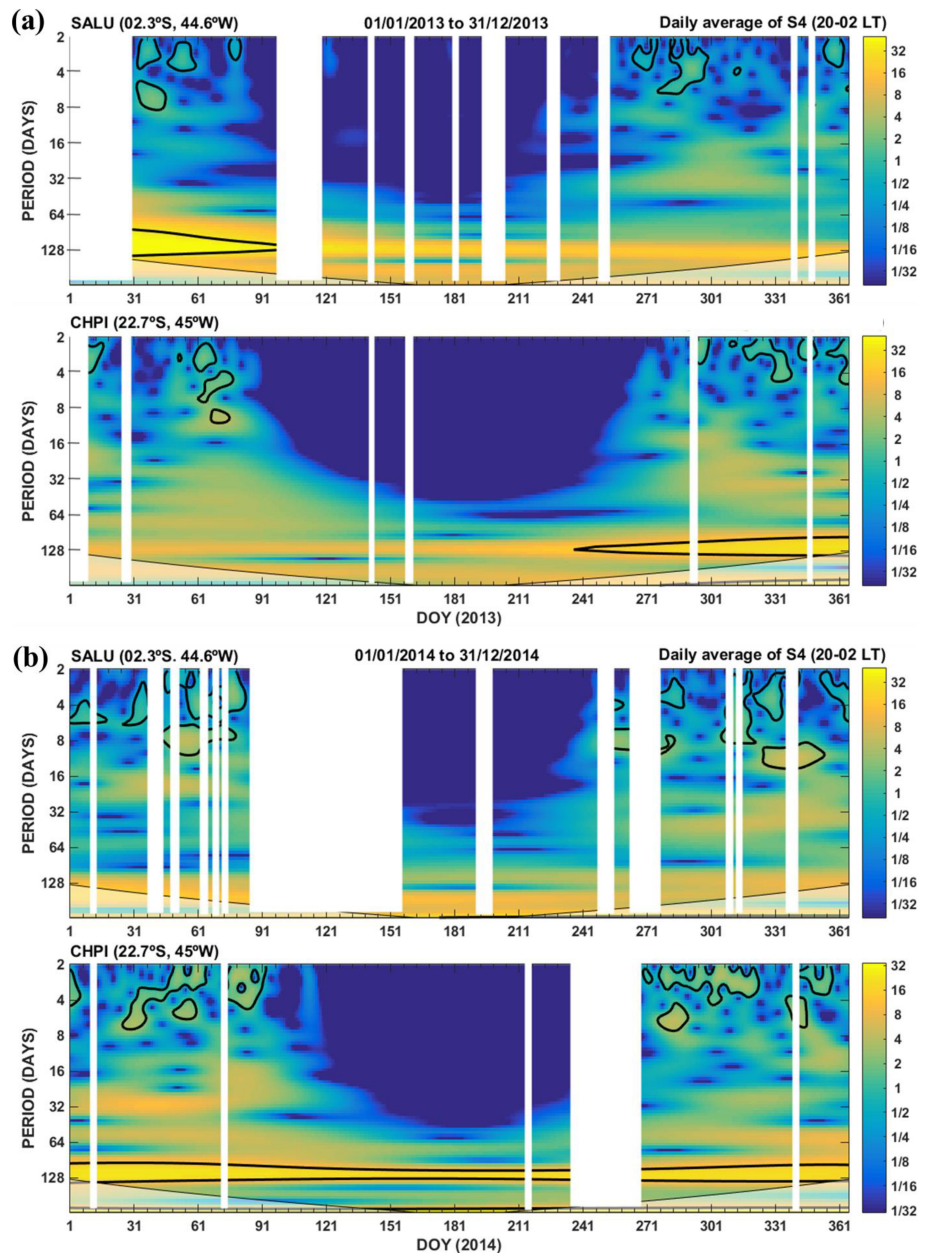


Figure 10. (a) Wavelet transform applied in the daily average of S4 during night hours (20–02 LT) of DOY 01 to 365 of 2013. The white bars indicate no data. (b) Same as Figure 10a but for 2014.

The plots presented in Figures 8, 9a, 9b, 10a, and 10b show that the period of ~64–128 days is intense in ROTI and S4 throughout the years 2013–2014. These types of oscillations probably have no influence on the formation of the ionospheric irregularities, since they are present in periods of absence in the occurrence of irregularities. As pointed out by Lastovicka et al. (2003) and Chang et al. (2011), propagating planetary waves are global-scale oscillations with typical periods of about 2–30 days. These waves are generated by random forcing events in the stratosphere and penetrate through the top of ionosphere (Aburjania et al., 2003; Bertoni et al., 2011; Forbes & Leveroni, 1992). Consequently, they modulate the equatorial ionosphere (Ogawa et al., 2009). In the present work, Figures 8 (on DOY ~280–331), 9a, 9b, 10a, and 10b (on DOY 270–90) show, for the first time, that planetary wave-scale periods ranging from ~2 to ~8 days are present simultaneously in ROTI and S4 during the strong phase fluctuations (ROTI >1) at 19 LT and 20–02 LT in the South American sector. We also note that during weak level of phase fluctuations (ROTI <0.4) in

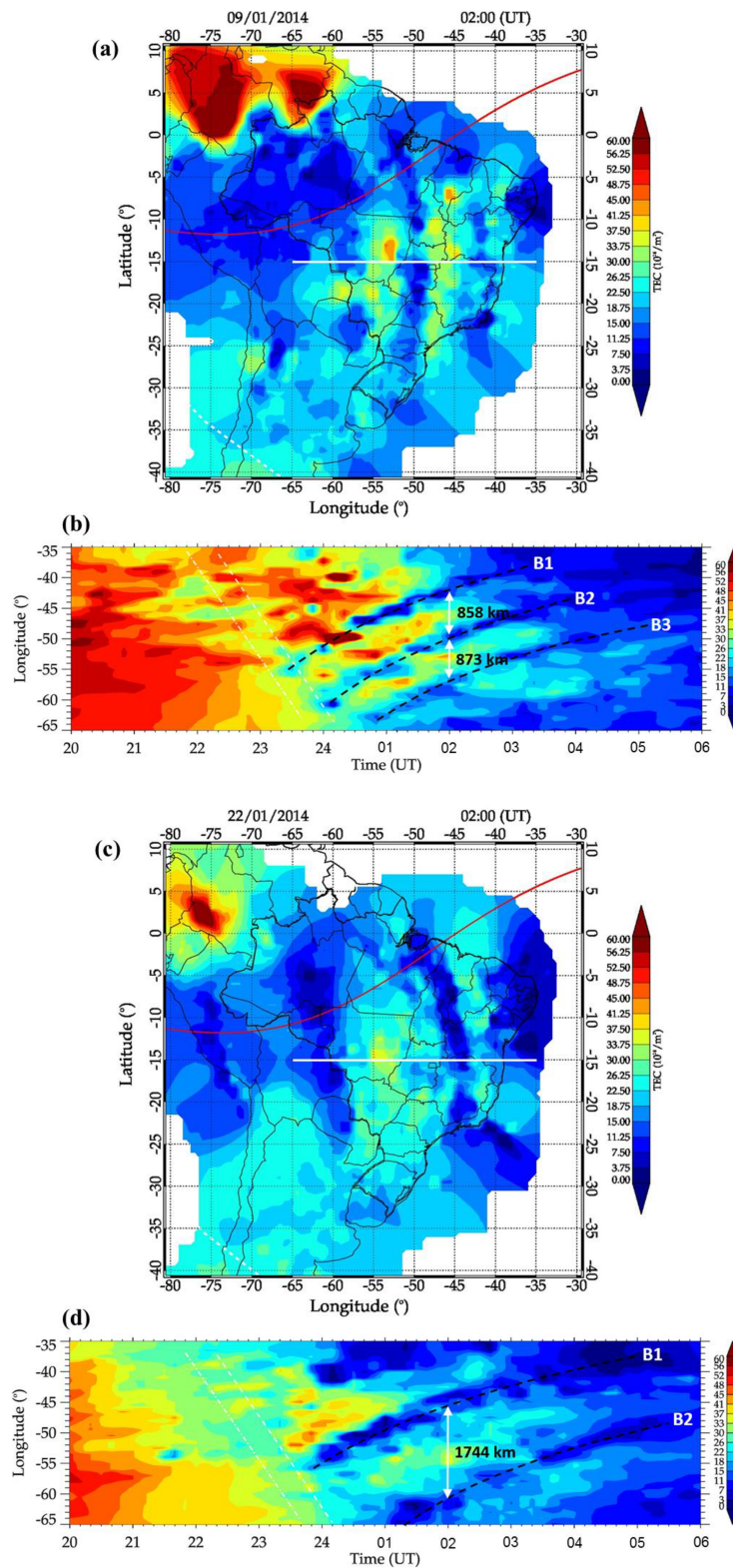


Figure 11. (a) TEC map over South American sector at 02 UT on 9 January 2014. The geomagnetic equator (red colored curve) is also shown. The horizontal white line represents the TEC data used to compute the interbubble distances at 15°S. The dashed white line indicates the solar terminator at 296-km height. (b) Keogram of TEC map over South America (15°S) from 35°W to 65°W, between 20 and 06 UT on the evening of 8–9 January 2014. The dashed black lines (B1–B3) indicate the plasma bubble locations in the keogram. The dashed and the dash-dotted white line represent the nautical and astronomical solar terminator at an altitude of 130 and 300 km, respectively. (c and d) Same as Figures 11a and 11b but for 22 January 2014.

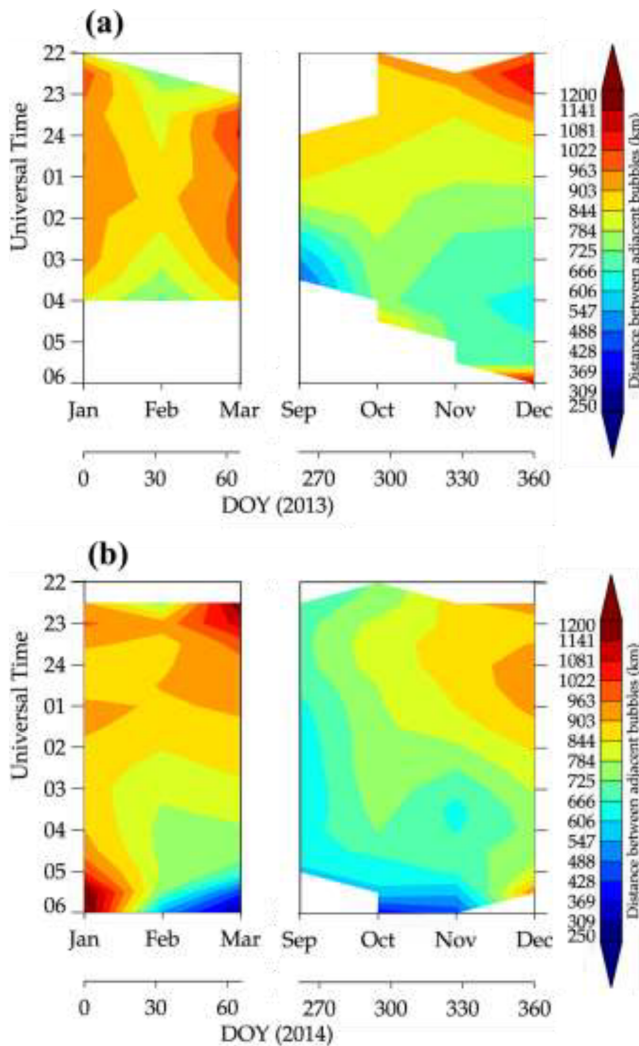


Figure 12. (a) Distance between adjacent ionospheric bubbles observed from GPS receivers spanning from $\sim 0^{\circ}\text{S}$ to $\sim 35^{\circ}\text{S}$ and from 35°W to 75°W over the South American sector during 2013. (b) Same as Figure 12a but for 2014.

from the TEC maps at 15°S and between 35°W and 65°W during 20–06 UT on 9 January 2014. The nautical (dashed white line) and astronomical (dash-dotted white line) solar terminator near 130- and 300-km altitude, respectively, are also shown in Figure 11b. Figures 11c and 11d are similar to Figures 11a and 11b, respectively, but for 22 January 2014. Figure 11a shows clearly three plasma bubbles (named B1–B3 in Figure 11b) at 02 UT on 9 January 2014. On this night at 02 UT (15°S), (1) the distance between depletions B1 and B2 is 858 km, and (2) the interbubble distance between B2 and B3 is 873 km. At least two plasma bubbles (named B1 and B2 in Figure 11d) can be recognized at 02 UT on 22 January 2014 in Figures 11c and 11d. On 22 January 2014, the interbubble distance at 02 UT (15°S) is 1,744 km.

Figures 12a and 12b show the distance between adjacent bubbles as a function of UT and DOY during 2013 and 2014, respectively. The distance between adjacent bubbles was not calculated during the period from ~ 5 March (DOY 64) to ~ 20 September (DOY 263), because the ionospheric irregularities rarely occurred in this period. Between 05 and 06 UT the results presented in Figures 12a and 12b are not reliable, because at this time possibly there is an error in the calculation of the distance between bubbles due to the little variation between the peak and valley of the TEC. The methodology used to calculate the distance between bubbles shows an uncertainty in the edges because of the low “delta TEC” (dTEC). The greater the difference

January and March at 19 LT (see Figure 3a) the main planetary wave-scale period is ranging from ~ 2 to ~ 4 days (see Figure 8). There is evidence of planetary waves modulating the thermospheric zonal wind speed and consequently controlling the ionosphere and upward $E \times B$ plasma drift (Abdu et al., 2006; de Abreu et al., 2014; Takahashi et al., 2006). Abdu et al. (2006) have reported that the planetary wave-scale oscillations in the evening prereversal enhancement of the equatorial electric field (PRE) generate strong modulation in the spread F (ionospheric irregularity). According to Abdu et al. (2006), considerations on the PRE development mechanism involving the E layer integrated conductivity including the effect of metallic ions and tidal winds demonstrated the source of the PRE oscillations to be planetary wave modulation of E region tidal winds. Onohara et al. (2013) simulated the effect of the ultrafast Kelvin waves in the F region vertical drift prereversal enhancement. They showed that ultrafast Kelvin waves in the mesosphere-low thermosphere region could modulate the vertical drift and explain the oscillations observed in the ionospheric parameters. Besides the planetary waves, there is growing evidence that the lunar semidiurnal tides have a great importance in the generation of spread F (e.g., Paulino et al., 2019). Using OI 630 nm all-sky imaging and coherent backscatter radar in the equatorial region over South America, Paulino et al. (2019) observed that a semimonthly oscillation due to quasi 16 days planetary waves and lunar semidiurnal tide can modulate the PRE responsible to generate ionospheric irregularities.

3.3. Adjacent Plasma Bubble Distance

Figure 1b shows a map with the GPS-TEC stations used to study the distance between adjacent plasma bubbles (also referred as interbubble distance). The distance between adjacent ionospheric plasma bubbles was computed using the TEC maps and keogram methods explained in a previous section. Examples of the TEC maps and keograms showing some of the plasma bubbles used to calculate the interbubble distances are shown in Figure 11.

Figure 11a depicts a TEC map over South America at 02 UT on the night of 9 January 2014. The horizontal white line highlights the TEC values located at 15°S . These TEC values were used to compute the interbubble distances at 15°S . The dashed white line indicates the solar terminator near 300-km height. Figure 11b shows a keogram generated

between a valley and peak of the TEC, the better the methodology performs to calculate the distance between adjacent bubbles. According to Barros et al. (2018), the ionospheric plasma bubbles observed in the TEC map were defined as (1) a TEC depletion with an amplitude exceeding 10 TECU and (2) a TEC perturbation with an extension of more than 500 km in the north-south direction.

As revealed from Figures 12a and 12b, the longitudinal distances between adjacent bubble depletions in January and February during 2013 and 2014 range from ~700 to 1,000 km around 22–05 UT, and the depletion with distances below ~850 km appears nearly 03–05 UT (2013–2014) and 22–24 UT (2013) mainly in February. It is also seen from Figures 12a and 12b that depletion with distances over 1,022 km appears between ~22 and 23 UT in February (2014), November, and December (2013). The temporal distribution (time-month) of the interbubble distances, greater than 1,022 km, is a first-of-its-kind observation reported in the literature, so far. Figure 12a shows that a prominent peak (over ~850 km) in the average distance between plasma bubbles appears near 22–24 UT in September, October, November, and December 2013. It is also clearly noticed from Figure 12a that the average distance between adjacent bubbles in September–December 2013 has a decreasing tendency from ~22 to ~05 UT. However, the plot presented in Figure 12b shows that the average distance between bubbles around 22–05 UT increased from September to December 2014, and the average distance between adjacent bubbles exceeds 850 km between ~23 and 02 UT in December. It is also seen from Figure 12b that the distances between adjacent bubbles range from ~600 to 1,000 km in September–December 2014. As far as we know, this is the first time that strongly distinct temporal gradients in the interbubble distance have been reported in consecutive years over South America. The interbubble distance is determined by the wavelength of the seeding gravity waves (Huang et al., 2013). Thus, the temporal gradient in the interbubble distances in South America observed in September–December is not so similar for years 2013 and 2014 possibly due to the different wavelengths of the gravity waves in each year. However, more case studies are necessary in order to be further substantiated.

Some works have studied the interbubble distance in the South American sector observed by all-sky imagers (Chapagain, 2011; Makela et al., 2010; Pautet et al., 2009; Takahashi et al., 2009) and GPS receivers (Takahashi et al., 2015, 2016; Barros et al., 2018). Pautet et al. (2009) investigated the ionospheric irregularities observed by two all-sky imagers over Brazil during September–November 2005 (a period of LSA) and reported that the majority of the adjacent plasma bubbles observed from Brasilia (14.8°S, 47.6°W) and Cariri (7.4°S, 36°W) exhibited separation of 100 to 200 km. Using data from Cariri and Brasilia, Takahashi et al. (2009) also reported on 30 September 2005 “OI 6300 depletions” with a distance of ~130 km between the adjacent structures. Using OI 630-nm all-sky imaging observations from Christmas Island (2.1°N, 157.4°W; during October 1994; a period of LSA) in the Central Pacific Ocean and Alcantara (2.3°S, 44.5°W; during September–October 1995; a period of LSA) in Brazil, Chapagain (2011) reported that the distance between adjacent bubbles ranges from ~150 to 250 km over Christmas Island and ~100 to 200 km over Alcantara. Using a field-aligned airglow imaging system over Chile (30.2°S, 70.8°W) between August 2006 and August 2009, Makela et al. (2010) reported that the mean spacing between consecutive plasma bubbles is ~290 km. The previous studies using all-sky imager clearly show that the average distance between plasma bubbles is lower than 350 km over South America. However, recent investigations about adjacent plasma bubble separation were made by Takahashi et al. (2015, 2016) and Barros et al. (2018) using GPS receivers over South America and reported interbubble distance greater than 400 km. Barros et al. (2018) investigated the characteristics of the equatorial plasma bubbles observed by TEC map over South America for the period between November 2012 and January 2016 and reported a latitudinal gradient ranging from 920 km at the magnetic equator to 640 km at 30°S. They also reported, for the first time, interbubble distance greater than 1,000 km on some nights. Interbubble distance greater than 400 km was also observed via satellite data (Huang et al., 2013; Lin et al., 2005). Using simultaneous observations of the equatorial ionosphere by ROCSAT-1 and IMAGE satellites, Lin et al. (2005) reported a separation distance between bubbles varying from 300 to 1,000 km. Adjacent plasma bubble separation ranging from 500 to 1,000 km was also detected by the Communication/Navigation Outage Forecasting System satellite (Huang et al., 2013). Our results showed that the distance between adjacent consecutive plasma bubbles ranges from ~600 to 1,000 km (in South America), in good agreement with the results presented by Lin et al. (2005), Huang et al. (2013), Takahashi et al. (2015, 2016), and Barros et al. (2018). Sinha and Raizada (2000) suggest that gravity waves might be the seeding agent for generating the separation between the adjacent plasma bubbles.

These results (in the present study) disagree with the observations in the South American sector during another period presented by Pautet et al. (2009), Takahashi et al. (2009), and Chapagain (2011). However, the present study is during the HSA while the reports on adjacent bubble separation by Pautet et al. (2009), Takahashi et al. (2009), and Chapagain (2011) are during LSA. Makela et al. (2010) reported that the average spacing between adjacent plasma bubbles decreases with the decrease in solar activity. According to Makela et al. (2010), this is associated with lower background temperatures during LSA, which does not allow easy propagation of the gravity waves with larger horizontal wavelength to plasma bubbles seeding heights. Although the solar activity has a great influence in the separation between the adjacent bubbles, this process alone is not enough to produce such a large difference in the interbubble distance as those observed by all-sky imagers and GPS receivers. All-sky imager has some limitations: (a) dependence on favorable weather conditions and (b) the airglow imaging data (within a diameter of $\sim 1,600$ km) cover a restricted area of $\sim 15^\circ$ of latitude and longitude (Takahashi et al., 2015). The advantage of the TEC map derived from GPS stations (used in this investigation) over previous techniques is that (a) it covers practically the whole of South America and consequently does not have the latitudinal and longitudinal limitations of the all-sky imager, and (b) the plasma bubbles can be monitored continuously independent of the local weather conditions. This suggests that our results differ from some previous investigations possibly due to the difference in the technique used to study the interbubble distance. The main mechanisms for the generation of the periodic structure of equatorial plasma bubbles have been proposed by Tsunoda et al. (2011), Huang et al. (2013), and Takahashi et al. (2018). As described by Tsunoda et al. (2011), the VTEC depletions are directly related to upwellings in large-scale wave structure. Tsunoda et al. (2011) further mentioned that seeding of large-scale wave structure occurs from a sequence of events, beginning with the excitation of atmospheric gravity waves (AGWs) in the troposphere or lower thermosphere, their propagation up to the thermosphere, and the transfer of AGW wind perturbations via neutral-ion coupling to the plasma at the base of the F layer. Huang et al. (2013) have proposed that the sunset terminator is the region where AGWs can be excited, and each cycle of gravity waves initiates a single plasma bubble. The results by Buhari et al. (2014) seem to confirm this assumption. Buhari et al. (2014) reported that 16 striations of equatorial plasma bubbles were generated continuously around the passage of the solar terminator on 5 April 2011 over southeast Asia. Huang et al. (2013) have concluded that a characteristic longitudinal separation of 500–1,000 km between adjacent bubbles corresponds to a temporal periodicity of 15–30 min of the seeding gravity waves. However, as mentioned by Takahashi et al. (2018; Figure 9), mesospheric gravity waves and medium-scale traveling ionospheric disturbances (MSTIDs) show a linear relationship with respect to equatorial plasma bubbles. Takahashi et al. (2018) observed simultaneous occurrences of mesospheric gravity waves and plasma bubbles, and their horizontal scale range was between 50 and 300 km. Takahashi et al. (2018) also reported that both MSTIDs and equatorial plasma bubbles have a range of variation between 300 and 1,000 km. A possible source of MSTIDs could be AGWs originated in the lower atmosphere (Takahashi et al., 2018, and references therein). Finally, taking into account the theories developed by previous investigators, there is a high probability that AGWs and MSTIDs are the main possible equatorial plasma bubble seeding processes that explain favorably the interbubble distances.

4. Conclusions

This paper presents a study of the ionospheric irregularities observed in the South American sector during 2 years of HSA (2013–2014), using GPS data from several receiving networks covering from the equatorial to the low-latitude regions. The main conclusions of this work can be summarized as follows.

1. The variations in ROTI and S4 indices showed that the ionospheric irregularities occur frequently between September and April (equinoctial and summer months) around 20–02 LT over the equatorial and low-latitude stations in South America. ROTI index also presented strong phase fluctuations (ROTI >1) in October and November at 19 LT. In winter months (May–August) no irregularities were seen over all stations in the South American sector.
2. To our best knowledge, this is the first time that the results from the wavelet transform applied simultaneously in ROTI and S4 showed oscillations with periods of about 2–8 days during the strong phase fluctuations (ROTI >1) in South America at 19 LT (October–November) and 20–02 LT (equinoctial and summer months). These oscillations are probably related to the propagating planetary waves with

periods of about 2–8 days. The ROTI values also showed predominantly periods of about 2–4 days during weak level of phase fluctuations (ROTI <4) at 19 LT related with planetary waves of the same period.

3. The distance between adjacent consecutive ionospheric plasma bubbles was in the range of 600–1,000 km in the South American sector. A novel feature of the present investigation is the temporal gradient in the interbubble distances in South America: (a) varying from ~1,000 km around 22–23 UT to ~600 km around 04–05 UT during September–December 2013; and (b) varying from ~600 km in September to ~900 km in December around 22–05 UT for year 2014. In January–February for years 2013 and 2014 the distance between adjacent bubbles was ~900 km around 00–02 UT and ~600–800 km around 03–05 UT. It is also reported for the first time that the interbubble distances over 1,022 km occur predominantly around 22–23 UT over South America.

Acknowledgments

Two of the authors, R. de Jesus and I. S. Batista, wish to express their sincere thanks to the Brazilian funding agency “Coordenação de Aperfeiçoamento de Pessoal de Nível Superior” (CAPES) for financial support. I. S. B. thanks CNPq, grants 405555/2018-0 and 302920/2014-5. One of the authors (K. V.) acknowledges the National Atmospheric Research Laboratory (NARL), Gadanki, India, for providing fellowship. E. R. de Paula acknowledges the support of CNPq through grant 310802/2015-6 and INCT GNSS-NavAer grants 2014/465648/2014-2 CNPq and 2017/50115-0 FAPESP. The authors thank Aslak Grinsted for making available the software package used in the continuous wavelet transform. We also thank the authorities of the Brazilian Network of Continuum Monitoring of GNSS System (RBMC; <ftp://geoftp.ibge.gov.br/RBMC/>), Low-Latitude Ionospheric Sensor Network (LISN; <http://lisn.igp.gov.br/>), Argentinian Network of Continuum Monitoring of Satellites (RAMSAC; <http://www.ign.gov.ar/NuestrasActividades/Geodesia/Ramsac/DescargaRinex>), International GNSS Service (IGS; <ftp://cddis.gsfc.nasa.gov/gps/data/daily/>), and EMBRACE/INPE program (<http://www2.inpe.br/climaespacial/portal/en/>) for kindly allowing us to use the GPS data. The TEC map values were downloaded online from EMBRACE (<http://www2.inpe.br/climaespacial/portal/en/>). Authors also express their sincere thanks to Goddard Space Flight Center (GSFC), NASA for providing the solar index $F_{10.7}$ data (<http://omniweb.gsfc.nasa.gov/form/dx1.html>). D. Barros and C. A. O. B. Figueiredo thank the Conselho Nacional de Desenvolvimento Científico e Tecnológico (CNPq) under contract 301211/2019-1 and Fundação de Amparo à Pesquisa do Estado de São Paulo (FAPESP) for kindly providing financial support through process number 2018/09066-8.

References

- Abalde, J. R., Sahai, Y., Fagundes, P. R., Becker-Guedes, F., Bittencourt, J. A., Pillat, V. G., et al. (2009). Day-to-day variability in the development of plasma bubbles associated with geomagnetic disturbances. *Journal of Geophysical Research*, *114*, A04304. <https://doi.org/10.1029/2008JA013788>
- Abdu, M. A., Batista, P. P., Batista, I. S., Brum, C. G. M., Carrasco, A. J., & Reinisch, B. W. (2006). Planetary wave oscillations in mesospheric winds, equatorial evening prereversal electric field and spread F . *Geophysical Research Letters*, *33*, L07107. <https://doi.org/10.1029/1005GL024837>
- Abdu, M. A., Bittencourt, J. A., & Batista, I. S. (1981). Magnetic declination control of the equatorial F region dynamo electric field development and spread F . *Journal of Geophysical Research*, *86*, 11443.
- Abdu, M. A., & Brum, C. G. M. (2009). Electrodynamics of the vertical coupling processes in the atmosphere-ionosphere system of the low latitude region. *Earth, Planets and Space*, *61*, 385–395.
- Abdu, M. A., Brum, C. G. M., Batista, I. S., Sobral, J. H. A., de Paula, E. R., & Souza, J. R. (2008). Solar flux effects on equatorial ionization anomaly and total electron content over Brazil: Observational results versus IRI representations. *Advances in Space Research*, *42*, 617–625.
- Abe, O. E., Rabiú, A. B., & Radicella, S. M. (2018). Longitudinal asymmetry of the occurrence of the plasma irregularities over African low-latitude region. *Pure and Applied Geophysics*. <https://doi.org/10.1007/s00024-018-1920-z>
- Aburjania, G. D., Jandieri, G. V., & Khantadze, A. G. (2003). Self-organization of planetary electromagnetic waves in the E -region of the ionosphere. *Journal of Atmospheric and Solar-Terrestrial Physics*, *65*, 661–671.
- Aggarwal, M., Joshi, H. P., Iyer, K. N., & Kwak, Y. S. (2013). Response of the EIA ionosphere to the 7-8 May 2005 geomagnetic storm. *Advances in Space Research*, *52*, 591–603.
- Aggarwal, M., Joshi, H. P., Iyer, K. N., Kwak, Y.-S., Lee, J. J., Chandra, H., & Cho, K. S. (2012). Day-to-day variability of equatorial anomaly in GPS-TEC during low solar activity period. *Advances in Space Research*, *49*, 1709–1720.
- Anderson, D. N. (1973). A theoretical study of the ionospheric F region equatorial anomaly—I. Theory. *Planetary and Space Science*, *21*(3), 409–419. [https://doi.org/10.1016/0032-0633\(73\)90040-8](https://doi.org/10.1016/0032-0633(73)90040-8)
- Appleton, E. V. (1946). Two anomalies in the ionosphere. *Nature*, *157*, 691. <https://doi.org/10.1038/157691a0>
- Balan, N., Bailey, G. J., Moffett, R. J., Sut, Y. Z., & Titherid, J. E. (1995). Modelling studies of the conjugate-hemisphere differences in ionospheric ionization at equatorial anomaly latitudes. *Journal of Atmospheric and Terrestrial Physics*, *57*(3), 279–292.
- Balan, N., Souza, J., & Bailey, G. J. (2018). Recent developments in the understanding of equatorial ionization anomaly: A review. *Journal of Atmospheric and Solar-Terrestrial Physics*, *171*, 3–11. <https://doi.org/10.1016/j.jastp.2017.06.020>
- Barros, D., Takahashi, H., Wrasse, C. M., & Figueiredo, C. A. O. B. (2017). Characteristics of ionospheric plasma bubbles observed by TEC maps in Brazilian sector. *Sociedade Brasileira de Geofísica*, *1-3*.
- Barros, D., Takahashi, H., Wrasse, C. M., & Figueiredo, C. A. O. B. (2018). Characteristics of equatorial plasma bubbles observed by TEC map based on ground-based GNSS receivers over South America. *Annales de Geophysique*, *36*, 91–100.
- Basu, S., & Basu, S. (1983). High resolution topside in situ data of electron densities and VHF/GHz scintillations in the equatorial region. *Journal of Geophysical Research*, *88*(A1), 403–415.
- Basu, S., Groves, K. M., Quinn, J. M., & Doherty, P. (1999). A comparison of TEC fluctuations and scintillations at Ascension Island. *Journal of Atmospheric and Solar-Terrestrial Physics*, *61*, 1219–1226.
- Batista, I. S., Abdu, M. A., & Bittencourt, J. A. (1986). Equatorial F region vertical plasma drifts: seasonal and longitudinal asymmetries in the American sector. *Journal of Geophysical Research*, *91*(A11), 12,055–12,064.
- Batista, I. S., Abdu, M. A., Carrasco, A. J., Reinisch, B. W., de Paula, E. R., Schuch, N. J., & Bertoni, F. (2008). Equatorial spread F and sporadic E -layer connections during the Brazilian Conjugate Point Equatorial Experiment—COPEX. *Journal of Atmospheric and Solar-Terrestrial Physics*, *70*, 1133–1143.
- Batista, I. S., Medeiros, R. T., Abdu, M. A., & Souza, J. R. (1996). Equatorial ionospheric vertical plasma drift model over the Brazilian region. *Journal of Geophysical Research*, *101*(A5), 10,887–10,892.
- Bertoni, F. C. P., Sahai, Y., Raulin, J.-P., Fagundes, P. R., Pillat, V. G., de Castro, C. G. G., & Lima, W. L. C. (2011). Equatorial spread- F occurrence observed at two near equatorial stations in the Brazilian sector and its occurrence modulated by planetary waves. *Journal of Atmospheric and Solar-Terrestrial Physics*, *73*, 457–463.
- Bhattacharyya, A., Kakad, B., Gurramp, P., Sripathi, S., & Sunda, S. (2017). Development of intermediate-scale structure at different altitudes within an equatorial plasma bubble: Implications for L-band scintillations. *Journal of Geophysical Research, Space Physics*, *122*, 1015–1030. <https://doi.org/10.1002/2016JA023478>
- Bhattacharyya, A., Kakad, B., Sripathi, S., Jeeva, K., & Nair, K. U. (2014). Development of intermediate scale structure near the peak of the F region within an equatorial plasma bubble. *Journal of Geophysical Research: Space Physics*, *119*, 3066–3076. <https://doi.org/10.1002/2013JA019619>
- Bires, A., Roininen, L., Damtie, B., Nigussie, M., & Vanhamäki, H. (2016). Study of TEC fluctuation via stochastic models and Bayesian inversion. *Radio Science*, *51*, 1772–1782. <https://doi.org/10.1002/2016RS005959>
- Booker, H. G., & Wells, H. W. (1938). Scattering of radio waves in the F -region of the ionosphere. *Terrestrial Magnetism and Atmospheric Electricity*, *43*, 249–256.

- Buhari, S. M., Abdullah, M., Hasbi, A. M., Otsuka, Y., Yokoyam, T., Nishioka, M., & Tsugawa, T. (2014). Continuous generation and two-dimensional structure of equatorial plasma bubbles observed by high-density GPS receivers in southeast Asia. *Journal of Geophysical Research: Space Physics*, *119*, 10,569–10,580. <https://doi.org/10.1002/2014JA020433>
- Burke, W. J., Gentile, L. C., Huang, C. Y., Valladares, C. E., & Su, S.-Y. (2004). Longitudinal variability of equatorial plasma bubbles observed by DMSP and ROCSAT-1. *Journal of Geophysical Research*, *109*, A12301. <https://doi.org/10.1029/2004JA010583>
- Burke, W. J., Gentile, L. C., Shomo, S. R., Roddy, P. A., & Pfaff, R. F. J. (2012). Images of bottomside irregularities observed at topside altitudes. *Journal of Geophysical Research*, *117*, A03332. <https://doi.org/10.1029/2011JA017169>
- Casty, C., Raible, C. C., Stocker, T. F., Wanner, H., & Luterbacher, J. (2007). A European pattern climatology 1766–2000. *Climate Dynamics*, *29*, 791–805. <https://doi.org/10.1007/s00382-007-0257-6>
- Cervera, M. A., & Thomas, R. M. (2006). Latitudinal and temporal variation of equatorial ionospheric irregularities determined from GPS scintillation observations. *Annales de Geophysique*, *24*, 3329–3341.
- Chang, L. C., Liu, J.-Y., & Palo, S. E. (2011). Propagating planetary wave coupling in SABER MLT temperatures and GPS TEC during the 2005/2006 austral summer. *Journal of Geophysical Research*, *116*, A10324. <https://doi.org/10.1029/2011JA016687>
- Chapagain, N. P. (2011). Dynamics of equatorial spread F using ground-based optical and radar measurements. A dissertation submitted in partial fulfillment of the requirements for the degree of doctor of philosophy in Physics. Utah State University, Logan, Utah. <https://digitalcommons.usu.edu/etd/897/>, <https://repositorio.igp.gov.pe/handle/IGP/4468>
- Cherniak, I., Krankowski, A., & Zakharenkova, I. (2018). ROTI maps: A new IGS ionospheric product characterizing the ionospheric irregularities occurrence. *GPS Solutions*, *22*–69. <https://doi.org/10.1007/s10291-018-0730-1>
- Cherniak, I., & Zakharenkova, I. (2017). New advantages of the combined GPS and GLONASS observations for high-latitude ionospheric irregularities monitoring: Case study of June 2015 geomagnetic storm. *Earth, Planets and Space*, *69*–66.
- Dashora, N., & Pandey, R. (2005). Observations in equatorial anomaly region of total electron content enhancements and depletions. *Annales Geophysicae*, *23*, 2449–2456.
- de Abreu, A. J., Fagundes, P. R., Bolzan, M. J. A., Gende, M., Brunini, C., de Jesus, R., et al. (2014). Traveling planetary wave ionospheric disturbances and their role in the generation of equatorial spread-F and GPS phase fluctuations during the last extreme low solar activity and comparison with high solar activity. *Journal of Atmospheric and Solar-Terrestrial Physics*, *117*, 7–19.
- De Paula, E. R., de Oliveira, C. B. A., Caton, R. G., Negreti, P. M., Batista, I. S., Martinon, A. R. F., et al. (2019). Ionospheric irregularity behavior during the September 6–10, 2017 magnetic storm over Brazilian equatorial–low latitudes. *Earth, Planets and Space*, *71*, 42. <https://doi.org/10.1186/s40623-019-1020-z>
- De Paula, E. R., Kherani, E. A., Abdu, M. A., Batista, I. S., Sobral, J. H. A., Kantor, I. J., et al. (2007). Characteristics of the ionospheric F-region plasma irregularities over Brazilian longitudinal sector. *Indian Journal of Radio & Space Physics*, *36*, 268–277.
- Deng, B., Huang, J., Liu, W., Xu, J., & Huang, L. (2013). GPS scintillation and TEC depletion near the northern crest of equatorial anomaly over South China. *Advances in Space Research*, *51*, 356–365.
- Divine, D. V., & Godtliebsen, F. (2007). Bayesian modeling and significant features exploration in wavelet power spectra. *Nonlinear Processes in Geophysics*, *14*, 79–88.
- Fejer, B. G., Scherliess, L., & de Paula, E. R. (1999). Effects of the vertical plasma drift velocity on the generation and evolution of equatorial spread F. *Journal of Geophysical Research*, *104*(A9), 19,859–19,869.
- Forbes, J. M., & Leveroni, S. (1992). Quasi 16-day oscillation in the ionosphere. *Geophysical Research Letters*, *19*(10), 981–984.
- Girardin, M. P., Tardif, J., & Flannigan, M. D. (2006). Temporal variability in area burned for the province of Ontario, Canada, during the past 200 years inferred from tree rings. *Journal of Geophysical Research*, *111*, D17108. <https://doi.org/10.1029/2005JD006815>
- Grinsted, A., Moore, J. C., & Jevrejeva, S. (2004). Application of the cross wavelet transform and wavelet coherence to geophysical time series. *Nonlinear Processes in Geophysics*, *11*, 561–566.
- Hajra, R., Chakraborty, S. K., Mazumdar, S., & Alex, S. (2012). Evolution of equatorial irregularities under varying electrodynamic conditions: A multitechnique case study from Indian longitude zone. *Journal of Geophysical Research*, *117*, A08331. <https://doi.org/10.1029/2012JA017808>
- Hoang, T. L., Abdu, M. A., MacDougall, J., & Batista, I. S. (2010). Longitudinal differences in the equatorial spread F characteristics between Vietnam and Brazil. *Advances in Space Research*, *45*, 351–360.
- Huang, C.-S., La BeaujardièRe, O., Roddy, P. A., Hunton, D. E., Ballenthin, J. O., Hairston, M. R., & Pfaff, R. F. (2013). Large-scale quasiperiodic plasma bubbles: C/NOFS observations and causal mechanism. *Journal of Geophysical Research, Space Physics*, *118*, 3602–3612. <https://doi.org/10.1002/jgra.50338>
- Huang, L., Wang, J., Jiang, Y., Huang, J., Chen, Z., & Zhao, K. (2014). A preliminary study of the single crest phenomenon in total electron content (TEC) in the equatorial anomaly region around 120°E longitude between 1999 and 2012. *Advances in Space Research*, *54*, 2200–2207.
- Kelley, M. C. (1989). Development and initiation of equatorial spread F. In R. Dmowska & J. R. Holton (Eds.), *The Earth's Ionosphere: Plasma physics and electrodynamics*, Int. Geophys. Ser. (Vol. 43, pp. 121–135). San Diego, CA: Academic.
- Khadka, S. M., Valladares, C. E., Sheehan, R., & Gerrard, A. J. (2018). Effects of electric field and neutral wind on the asymmetry of equatorial ionization anomaly. *Radio Science*, *53*, 683–697. <https://doi.org/10.1029/2017RS006428>
- Langley, R., Fedrizzi, M., Paula, E., Santos, M., & Komjathy, A. (2002). Mapping the low latitude ionosphere with GPS. *GPS World*, *13*(2), 41–46.
- Lastovicka, J., Krizan, P., Sauli, P., & Novotna, D. (2003). Persistence of the planetary wave type oscillations in foF2 over Europe. *Annales de Geophysique*, *1543*–1552.
- Lin, C. S., Immel, T. J., Yeh, H.-C., Mende, S. B., & Burch, J. L. (2005). Simultaneous observations of equatorial plasma depletion by IMAGE and ROCSAT-1 satellites. *Journal of Geophysical Research*, *110*, A06304. <https://doi.org/10.1029/2004JA010774>
- Liu, G., Huang, W., Gong, J., & Shen, H. (2013). Seasonal variability of GPS-VTEC and model during low solar activity period (2006–2007) near the equatorial ionization anomaly crest location in Chinese zone. *Advances in Space Research*, *51*, 366–376.
- Ma, G., & Maruyama, T. (2006). A super bubble detected by dense GPS network at East Asian longitudes. *Geophysical Research Letters*, *33*, L21103. <https://doi.org/10.1029/2006GL027512>
- Makela, J. J., Vadas, S. L., Muryanto, R., Duly, T., & Crowley, G. (2010). Periodic spacing between consecutive equatorial plasma bubbles. *Geophysical Research Letters*, *37*, L14103. <https://doi.org/10.1029/2010GL043968>
- Manju, G., Haridas, M. K. M., & Aswathy, R. P. (2016). Role of gravity wave seed perturbations in ESF day-to-day variability: A quantitative approach. *Advances in Space Research*, *57*, 1021–1028.
- Mannucci, A. J., Wilson, B. D., & Edwards, C. D. (1993). A new method for monitoring the Earth's ionospheric total electron content using the GPS global network. Proc. of ION GPS-93 (pp. 1323–1332). Inst. of Navigation, Salt Lake City, Utah.

- Mendillo, M., Baumgardner, J., Pi, X., Sultan, P. J., & Tsunoda, R. (1992). Onset conditions for equatorial spread *F*. *Journal of Geophysical Research*, *97*, 13,865–13,876.
- Moffett, R. J., & Hanson, W. B. (1965). Effect of ionization transport on the equatorial *F*-region. *Nature*, *206*(4985), 705–706. <https://doi.org/10.1038/206705a0>
- Muella, M. T. A. H., de Paula, E. R., Kantor, I. J., Rezende, L. F. C., & Smorigo, P. F. (2009). Occurrence and zonal drifts of small-scale ionospheric irregularities over an equatorial station during solar maximum—Magnetic quiet and disturbed conditions. *Advances in Space Research*, *43*, 1957–1973.
- Muella, M. T. A. H., de Paula, E. R., & Monteiro, A. A. (2013). Ionospheric scintillation and dynamics of Fresnel-scale irregularities in the inner region of the equatorial ionization anomaly. *Surveys in Geophysics*, *34*(2), 233–251. <https://doi.org/10.1007/s10712-012-9212-0>
- Muella, M. T. A. H., Duarte-Silva, M. H., Moraes, A. O., de Paula, E. R., Rezende, L. F. C., Alfonsi, L., & Affonso, B. J. (2017). Climatology and modeling of ionospheric scintillations and irregularity zonal drifts at the equatorial anomaly crest region. *Annales de Geophysique*, *35*, 1201–1218.
- Ogawa, T., Miyoshi, Y., Otsuka, Y., Nakamura, T., & Shiokawa, K. (2009). Equatorial GPS ionospheric scintillations over Kototabang, Indonesia and their relation to atmospheric waves from below. *Earth, Planets and Space*, *61*, 397–410.
- Olwendo, O. J., Baluku, T., Baki, P., Cilliers, P. J., Mito, C., & Doherty, P. (2013). Low latitude ionospheric scintillation and zonal irregularity drifts observed with GPS-SCINDA system and closely spaced VHF receivers in Kenya. *Advances in Space Research*, *51*(9), 1715–1726.
- Onohara, A. N., Batista, I. S., & Takahashi, H. (2013). The ultra-fast Kelvin waves in the equatorial ionosphere: Observations and modeling. *Annales de Geophysique*, *31*, 209–215.
- Otsuka, Y., Shiokawa, K., & Ogawa, T. (2006). Equatorial ionospheric scintillations and zonal irregularity drifts observed with closely spaced GPS receivers in Indonesia. *Journal of the Meteorological Society of Japan*, *84*A, 343–351.
- Paulino, I., Medeiros, A. F., Buriti, R. A., Takahashi, H., Sobra, J. H. A., & Gobbi, D. (2011). Plasma bubble zonal drift characteristics observed by airglow images over Brazilian tropical region. *Revista Brasileira de Geofísica*, *29*(2), 239–246.
- Paulino, I., Paulino, A. R., de la Cruz Cueva, R. Y., Ageyi-Yeboah, E., Buriti, R. A., Takahashi, H., et al. (2019). Semimonthly oscillation observed in the start time of equatorial Spread-*F*. *Annals of Geophysics Discussions*. <https://doi.org/10.5194/angeo-2019-62>
- Pautet, P.-D., Taylor, M. J., Chapagain, N. P., Takahashi, H., Medeiros, A. F., São Sabbas, F. T., & Fritts, D. C. (2009). Simultaneous observations of equatorial *F*-region plasma depletions over Brazil during the Spread *F* experiment (SpreadFEx). *Annales de Geophysique*, *27*, 2371–2381.
- Pi, X., Mannucci, A. J., Lindqwister, U. J., & Ho, C. M. (1997). Monitoring of global ionospheric irregularities using the worldwide GPS network. *Geophysical Research Letters*, *24*(18), 2283–2286.
- Ram, S. T., Rao, P. V. S. R., Niranjan, K., Prasad, D. S. V. V. D., Sridharan, R., Devasia, C. V., & Ravindran, S. (2006). The role of post-sunset vertical drifts at the equator in predicting the onset of VHF scintillations during high and low sunspot activity years. *Annales de Geophysique*, *24*, 1609–1616.
- Rao, P. V. S. R., Krishna, S. G., Niranjan, K., & Prasad, D. S. V. V. D. (2006). Temporal and spatial variations in TEC using simultaneous measurements from the Indian GPS network of receivers during the low solar activity period of 2004–2005. *Annales de Geophysique*, *24*, 3279–3292.
- Sahai, Y., Fagundes, P. R., & Bittencourt, J. A. (2000). Transequatorial *F*-region ionospheric plasma bubbles: solar cycle effects. *Journal of Atmospheric and Terrestrial Physics*, *62*, 1377–1383.
- Sahai, Y., Fagundes, P. R., Bittencourt, J. A., & Abdu, M. A. (1998). Occurrence of large scale equatorial *F*-region plasma depletions during geo-magnetic disturbances. *Journal of Atmospheric and Solar-Terrestrial Physics*, *60*(16), 1593–1604.
- Sinha, H. S. S., & Raizada, S. (2000). Some new features of ionospheric plasma depletions over the Indian zone using all sky optical imaging. *Earth, Planets and Space*, *52*, 549–559.
- Sobral, J. H. A., Abdu, M. A., Takahashi, H., Taylor, M. J., de Paula, E. R., Zamlutti, C. J., et al. (2002). Ionospheric plasma bubble climatology over Brazil based on 22 years (1977–1998) of 630 nm airglow observations. *Journal of Atmospheric and Solar - Terrestrial Physics*, *64*, 1517–1524.
- Sripathi, S., Kakad, B., & Bhattacharyya, A. (2011). Study of equinoctial asymmetry in the Equatorial Spread *F* (ESF) irregularities over Indian region using multi-instrument observations in the descending phase of solar cycle 23. *Journal of Geophysical Research*, *116*, A11302. <https://doi.org/10.1029/2011JA016625>
- Stolle, C., Manoj, C., Luhr, H., Maus, S., & Alken, P. (2008). Estimating the daytime equatorial ionization anomaly strength from electric field proxies. *Journal of Geophysical Research*, *113*, A09310. <https://doi.org/10.1029/2007JA012781>
- Takahashi, H., Taylor, M. J., Pautet, P.-D., Medeiros, A. F., Gobbi, D., Wrasse, C. M., et al. (2009). Simultaneous observation of ionospheric plasma bubbles and mesospheric gravity waves during the SpreadFEx campaign. *Annales de Geophysique*, *27*, 1477–1487.
- Takahashi, H., Wrasse, C., Denardini, C., Pádua, M., Paula, E., Costa, S., et al. (2016). Ionospheric TEC weather map over South America. *Advances in Space Research*, *14*, 937–949.
- Takahashi, H., Wrasse, C. M., Figueiredo, C. A. O. B., Barros, D., Abdu, M. A., Otsuka, Y., & Shiokawa, K. (2018). Equatorial plasma bubble seeding by MSTIDs in the ionosphere. *Progress in Earth and Planetary Science*, 5–32. <https://doi.org/10.1186/s40645-018-0189-2>
- Takahashi, H., Wrasse, C. M., Otsuka, Y., Ivo, A., Gomes, V., Paulino, I., et al. (2015). Plasma bubble monitoring by TEC map and 630 nm airglow image. *Journal of Atmospheric and Solar - Terrestrial Physics*, *130*, 151–158.
- Takahashi, H., Wrasse, C. M., Pancheva, D., Abdu, M. A., Batista, I. S., Lima, L. M., et al. (2006). Signatures of 3–6 day planetary waves in the equatorial mesosphere and ionosphere. *Annales Geophysicae*, *24*, 3343–3350. <https://doi.org/10.5194/angeo-24-3343-2006>
- Tanna, H. J., & Pathak, K. N. (2014). Longitude dependent response of the GPS derived ionospheric ROTI to geomagnetic storms. *Astrophysics and Space Science*, *352*, 373–384.
- Thébault, E., Finlay, C. C., Beggan, C. D., Alken, P., Aubert, J., Barrois, O., et al. (2015). International Geomagnetic Reference Field: The 12th generation. *Earth, Planets and Space*. <https://doi.org/10.1186/s40623-015-0228-9>
- Torrence, C., & Compo, G. P. (1998). A practical guide to wavelet analysis. *Bulletin of the American Meteorological Society*, *79*, 61–78.
- Trivedi, R., Jain, A., Jain, S., & Gwal, A. K. (2011). Study of TEC changes during geomagnetic storms occurred near the crest of the equatorial ionospheric ionization anomaly in the Indian sector. *Advances in Space Research*, *48*, 1617–1630.
- Tsunoda, R. T. (1985). Control of the season and longitudinal occurrence of equatorial scintillations by the longitudinal gradient in integrated *F* region Pederson conductivity. *Journal of Geophysical Research*, *90*, 447–456.
- Tsunoda, R. T., Yamamoto, M., Tsugawa, T., Hoang, T. L., Tulasi Ram, S., Thampi, S. V., et al. (2011). On seeding large-scale wave structure equatorial spread *F* and scintillations over Vietnam. *Geophysical Research Letters*, *38*, L20102. <https://doi.org/10.1029/2011GL049173>

- Uma, G., Liu, J. Y., Chen, S. P., Sun, Y. Y., Brahmanandam, P. S., & Lin, C. H. (2012). A comparison of the equatorial spread F derived by the International Reference Ionosphere and the S4 index observed by FORMOSAT-3/COSMIC during the solar minimum period of 2007–2009. *Earth, Planets and Space*, *64*, 467–471.
- Wang, G. J., Shi, J. K., Wang, X., & Shang, S. P. (2008). Seasonal variation of spread- F observed in Hainan. *Advances in Space Research*, *41*, 639–644.
- Wattanasangmechai, K., Yamamoto, M., Saito, A., Maruyama, T., Yokoyama, T., Nishioka, M., & Ishii, M. (2015). Temporal change of EIA asymmetry revealed by a beacon receiver network in Southeast Asia. *Earth, Planets and Space*, *67*(1), 1–12. <https://doi.org/10.1186/s40623-015-0252-9>
- Whalen, J. A. (1997). Equatorial bubbles observed at the north and south anomaly crests: Dependence on season, local time and dip latitude. *Radio Science*, *32*, 1559–1566.
- Whalen, J. A. (2000). An equatorial bubble: Its evolution observed in relation to bottomside spread F and to the Appleton anomaly. *Journal of Geophysical Research*, *105*, 5303–5315.
- Whalen, J. A. (2001). The equatorial anomaly: Its quantitative relation to equatorial bubbles, bottomside spread F and $E \times B$ drift velocity during a month at solar maximum. *Journal of Geophysical Research*, *106*, 29,125–29,132.
- Whalen, J. A. (2002). Dependence of equatorial bubbles and bottom side spread F on season, magnetic activity, and $E \times B$ drift velocity during solar maximum. *Journal of Geophysical Research*, *107*(A2), 1024. <https://doi.org/10.1029/2001JA000039>
- Whalen, J. A. (2009). The linear dependence of GHz scintillation on electron density observed in the equatorial anomaly. *Annales de Geophysique*, *27*, 1755–1761.
- Yeh, K. C., & Liu, C. H. (1982). Radio wave scintillations in the ionosphere. *Proceedings IEEE*, *70*, 324–360.
- Zhang, M.-L., Wan, W., Liu, L., & Ning, B. (2009). Variability study of the crest-to-trough TEC ratio of the equatorial ionization anomaly around 120° E longitude. *Advances in Space Research*, *43*, 1762–1769.
- Zhenzhong, X., Weimin, W., Ren, Z., & Shenggao, Y. (2012). Variation of ionospheric total electron content at crest of equatorial anomaly in China from 1997 to 2004. *Advances in Space Research*, *49*(3), 539–545.
- Zou, Y. (2011). Ionospheric scintillations at Guilin detected by GPS ground-based and radio occultation observations. *Advances in Space Research*, *47*, 945–965.
- Zou, Y., & Wang, D. (2009). A study of GPS ionospheric scintillations observed at Guilin. *Journal of Atmospheric and Solar-Terrestrial Physics*, *71*, 1948–1958.